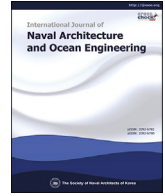


Contents lists available at [ScienceDirect](#)

## International Journal of Naval Architecture and Ocean Engineering

journal homepage: <http://www.journals.elsevier.com/international-journal-of-naval-architecture-and-ocean-engineering/>

# Nonlinear URANS model for evaluating course keeping and turning capabilities of a vessel with propulsion system failure in waves

Daejeong Kim <sup>a,\*</sup>, Soonseok Song <sup>a</sup>, Tonio Sant <sup>b</sup>, Yigit Kemal Demirel <sup>a</sup>, Tahsin Tezdogan <sup>a</sup><sup>a</sup> Department of Naval Architecture, Ocean and Marine Engineering, University of Strathclyde, Glasgow, UK<sup>b</sup> Department of Mechanical Engineering, Faculty of Engineering, University of Malta, Msida, Malta

## ARTICLE INFO

## Article history:

Received 23 August 2021

Received in revised form

15 November 2021

Accepted 16 November 2021

Available online 19 November 2021

## Keywords:

Ship manoeuvrability

Seakeeping

Course-keeping control

Computational Fluid Dynamics (CFD)

KRISO Container Ship (KCS)

Propulsion loss

## ABSTRACT

The loss of ship propulsion has been reported to be the most frequent cause of accidents at sea over the last few years. The loss of propulsive power has a notable effect on the behaviour of a ship during ship manoeuvring, and hence the manoeuvrability of ships suffering from propulsion loss should be accurately estimated for navigation safety. The aim of this study is to evaluate the effects of a propulsion failure on the manoeuvrability of the KRISO Container Ship (KCS) using a fully nonlinear URANS model, which is capable of resolving complex fluid-structure interactions with high accuracy. A series of case studies were carried out to compare the ship performances of both the normal and propulsion loss condition, especially for the course keeping and turning circle manoeuvres. The results explicitly revealed that the propulsion failure has a strong influence on the ship manoeuvrability, implying the importance of sufficient propulsion power when vessels are underway. The key findings obtained from this study are believed to provide navigators with a practical insight into ship manoeuvrability under the propulsion failure condition as well as contribute to developing standards for navigational safety in waves.

© 2021 Society of Naval Architects of Korea. Production and hosting by Elsevier B.V. This is an open access article under the CC BY-NC-ND license (<http://creativecommons.org/licenses/by-nc-nd/4.0/>).

## 1. Introduction

With a growing reliance on shipping activities, the ever-increasing maritime traffic has posed a considerable threat to navigational safety at sea. According to a marine accident investigation (EMSA, 2020), the most frequent cause of accidents over 2014–2019 was reported to be “Loss of control – Loss of propulsion power” which accounted for 22% of all casualty events reported, as shown in Fig. 1. This type of incident was also examined to be mainly related to commercial cargo ships. The loss of ship propulsion is one of the most hazardous events observed in marine transportation since it has a strong adverse effect on a ship's manoeuvrability in real sea states. Such poor ship manoeuvrability in areas of high-density traffic or narrow waterways could lead to further serious navigation casualties associated with collision, contact, and grounding incidents. Considering these potential dangers, predicting the manoeuvring performance of a vessel in case of any propulsion loss is critical for proper decision-making

about ship handling to ensure navigation safety at sea. It is of note that the Port State Control (PSC) has categorised the propulsion failure into the critical deficiency items which are not in compliance with inspection standards and thus cause the detention of the ship (IMO, 2020). In practice, the Port State Control Officers (PSCOs) carry out the inspection of foreign ships by the port governing states to verify the condition of the vessel, ensure the equipment onboard complies with the requirements of international conventions and that the vessel is manned and operated in accordance with international law.

The manoeuvring behaviour of a ship is highly dependent on the propulsion power (Hasnan et al., 2019). A study by Yasukawa and Yoshimura (2015) identified the rudder inflow velocity induced by a rotating propeller as a key parameter to determine the rudder normal force which directly affects the steering capability. The greater inflow velocity leads to the larger rudder normal force which then guarantees good manoeuvrability. Hence, the failure of the propulsion system is expected to adversely influence a ship's manoeuvring performance by decreasing the inflow velocity to the rudder, and consequently the sufficient rudder force cannot be achieved. All commercial vessels are likely to experience the propulsion loss incident which commonly results from the main

\* Corresponding author.

E-mail address: [daejeong.kim@strath.ac.uk](mailto:daejeong.kim@strath.ac.uk) (D. Kim).

Peer review under responsibility of The Society of Naval Architects of Korea.

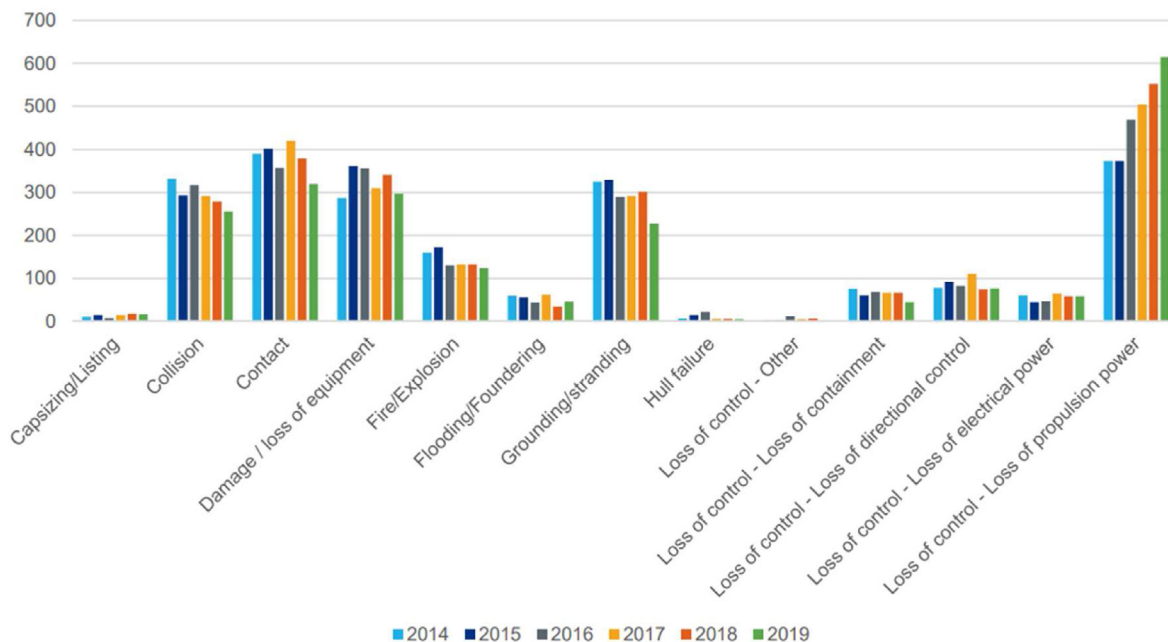


Fig. 1. Distribution of casualty events with a ship over the period 2014–2019, adapted from EMSA (2020).

engine failure. Considering this, navigation officers who are responsible for ship handling and navigation should be fully acquainted with the ship's manoeuvrability in the propulsion failure condition to ensure navigation safety at sea. These points underlie the main argument of this study, that the investigation into the relationship between the propulsion failure and the manoeuvring performance of commercial ships in real sea states is necessary.

In general, System Based (SB) methods, experimental methods, or both, are currently being used to estimate the manoeuvring performance of ships. The SB approaches involve performing manoeuvring simulations by solving the simplified mathematical model. Two distinctive mathematical models have been mainly used, such as the Abkowitz model (Abkowitz, 1964) and the Manoeuvring Modelling Group (MMG) model (Inoue et al., 1981; Yasukawa and Yoshimura, 2015). These mathematical models require a full set of hydrodynamic derivatives that need to be acquired from captive model tests or semi-empirical formulas. As mathematical models are combined with the potential flow theory, the manoeuvring behaviours of ships in waves could be extensively studied. Examples include the works of Skejic and Faltinsen (2008); Seo and Kim (2011); Subramanian and Beck (2015); (Zhang and Zou, 2016); Paroka et al. (2017); Zhang et al. (2017). A major advantage of the SB methods is that they are not time-consuming in terms of performing the manoeuvring simulation. However, the accuracy of these mathematical models may be limited due to uncertainties in the hydrodynamic coefficients (Mofidi and Carrica, 2014). Moreover, the complex interactions between the hull, rudder, and propeller are very difficult to precisely capture which could diminish the calculation accuracy.

In addition to the captive model tests for the SB methods, free-running model tests also have an important role in experimental-based research. These manoeuvring tests with free-running models are capable of predicting the manoeuvring performance of a ship in a direct way. This has been in general accepted as the most reliable approach. To date, a number of researchers have attempted to conduct free-running tests in calm water to evaluate the manoeuvring qualities including turning, yaw checking, and

course keeping ability according to the IMO requirements (ITTC, 2021). Although predicting the manoeuvring performance of a ship in calm water has almost become an industry standard (Shigunov, 2019), it cannot represent a ship's manoeuvrability in real sea states. With the increasing demand for estimating the ship's manoeuvring behaviour in waves (IMO, 2014; ITTC, 2017), several authors have conducted the ship manoeuvring analysis in waves for various ship types, for example, the Office of Naval Research Tumblehome (ONRT) ship (Sanada et al., 2013, 2019; Elshiekh, 2014), the KRISO Very Large Crude-oil Carrier 2 (KVLCC2) (Kim et al., 2019), and the KRISO Container Ship (KCS) (Yasukawa et al., 2021). However, it requires a large wave basin, manoeuvring control units, and other measurement devices as well as it is time-consuming and cost-intensive. Due to these hindrances, only a few research organisations have been able to conduct free-running manoeuvre tests in waves.

Meanwhile, with continuing advances in computational power, Computational Fluid Dynamics (CFD) has been increasingly used as a means of estimating the manoeuvring performance of a ship. The main advantage of the CFD method is that both nonlinear and viscous effects can be incorporated and therefore it is capable of accurately resolving the complex fluid-structure interactions. There are two types of CFD approaches to evaluate the manoeuvring characteristics of a ship. One is to carry out the virtual captive model tests such as the Planar Motion Mechanism (PMM) or the Circular Motion Test (CMT) from which the manoeuvring hydrodynamic coefficients can be obtained for the SB method (Otzen and Simonsen, 2014; Hajivand and Mousavizadegan, 2015; He et al., 2016; Liu et al., 2018). However, as stated previously, the simplified mathematical models for the SB approach cannot accurately resolve the interactions between hull, propeller, and rudder during manoeuvring. Another CFD application is the free-running simulations of standard manoeuvres with rotating propeller(s) and steering rudders(s), which have become a highly robust tool to predict a ship's manoeuvrability. Several researchers have initially attempted to conduct CFD free-running manoeuvres to predict the manoeuvring performance of a ship in calm water (Mofidi and Carrica, 2014; Broglia et al., 2015; Shen et al., 2015; Wang et al.,

2016). The studies in this area verified the reliability of the CFD simulations with free-running ship models by showing good agreement between CFD results and the experimental data available. More recently, researchers have started to focus on the ship's manoeuvrability in various wave conditions by applying the Stokes wave models (Wang et al., 2017, 2018; Wang and Wan, 2018; Liu et al., 2020; Kim et al., 2021a, 2021b, 2021c).

The numerous academic studies described above only addressed the ship's manoeuvrability in normal operating conditions in which all machinery related to the navigation system are working properly. It is an undeniable fact that the past studies have the advantage of being informative in confirming the manoeuvring performance of ships in normal conditions. However, they were not able to offer insight into the understanding of the ship's manoeuvrability under the propulsion failure event in which a rotating propeller should be suddenly in a non-rotating state during manoeuvring. Given the importance of this issue and the lack of previous studies, this paper was motivated to investigate the manoeuvring performance of the well-known benchmarking KCS in the propulsion system failure. In this work, the free-running CFD model was developed using a commercial CFD software package. This paper aims to provide a better understanding of a ship's manoeuvrability experiencing a failed propulsion system in real sea conditions.

## 2. Methodology

This section will present the research methodology used in this paper, with the detailed description of the procedure in the included sub-sections. As shown in Fig. 2, the research methodology applied in this study comprises four main parts to assess the ship's manoeuvrability in the propulsion failure: 1) goal and scope, 2) numerical modelling, 3) execution of free running simulations, and 4) results of analysis. The first step dealt with the overall research aim and the selection of the analysis scope including the type of the ship and environmental conditions. The second step was proposed to perform the numerical setup of the free-running CFD model in different environmental and operating conditions. In the third step, the self-propulsion computations in calm water and waves were first carried out to reach the target surge speed. Subsequently, the propulsion failure conditions were achieved as the revolution of the rotating actuator disk was forced to change abruptly based on a propeller controller. Then, two representative free-running manoeuvres were performed, namely, course-keeping and standard turning circle manoeuvres. In the fourth step, all of the results from this study including the important hydrodynamic features and the

critical manoeuvring indices were demonstrated and discussed in detail.

### 2.1. Goal and scope

This paper is aimed to enhance the general understanding of the manoeuvring performance when the ship experiences the propulsion failure event during manoeuvring in calm water and waves. Although many types of manoeuvring tests are required to be performed to evaluate the overall ship's manoeuvrability by ITTC (2021), the focus of this study was placed on performing two representative free-running manoeuvres, i.e., the course keeping control and the turning capability. The KRISO Container Ship (KCS) appended with an actuator disk and a semi-balanced horn rudder was used in this paper's free-running simulations. Table 1 shows the main particulars of the KCS model (scale factor of 75.24) which has a very similar hull geometry to commercial container ships, implying the results will provide critical information on how propulsion loss affects the manoeuvring performance of real commercial container ships.

As previously stated, the self-propulsion computations should be initially conducted before the selected free-running manoeuvres in the propulsion failure condition. As shown in Table 2, the self-propulsion simulations were performed in six environmental conditions which cover the whole range of important wave directions: 1) calm water, 2) head wave, 3) bow wave, 4) beam wave, 5) quartering wave, and 6) following wave. Throughout all the wave cases (case2 – case6), a wave with height  $H = 0.048$  m and period  $T = 1.4$ s in the model scale was applied, which correspond to a wave height of 3.61 m and period of 12.14s in full scale. The wavelength equals to the ship length ( $\lambda/L_{BP} = 1.0$ ) and wave steepness ( $H/\lambda$ ) is 0.016. The encounter frequency of the wave,  $\omega_e$ , was calculated by means of  $\omega_e = \omega[1 - (\omega U \cos \mu)/g]$ , where  $\omega$  indicates the wave frequency,  $U$  indicates the ship surge speed,  $\mu$  means the ship's heading angle relative to the wave direction, and  $g$  is the gravitational acceleration. All the self-propulsion simulations adopted the propeller revolution rate (RPS) of 13.38 n/sec ( $n$  is the rotational speed of the propeller), which is the same propeller speed as that applied for the manoeuvring research of the KCS (the same scale factor of 75.24) in the literature (Kim et al., 2021c). Fig. 3 shows the schematic illustration for the simulation cases applied to this study, which includes the course keeping and turning circle manoeuvres either in calm water or in the presence of regular waves. After the self-propulsion conditions were achieved, the rotational speed of the actuator disk was compelled to decrease suddenly from 13.38 n/sec to 0 n/sec according to the propeller speed controller.

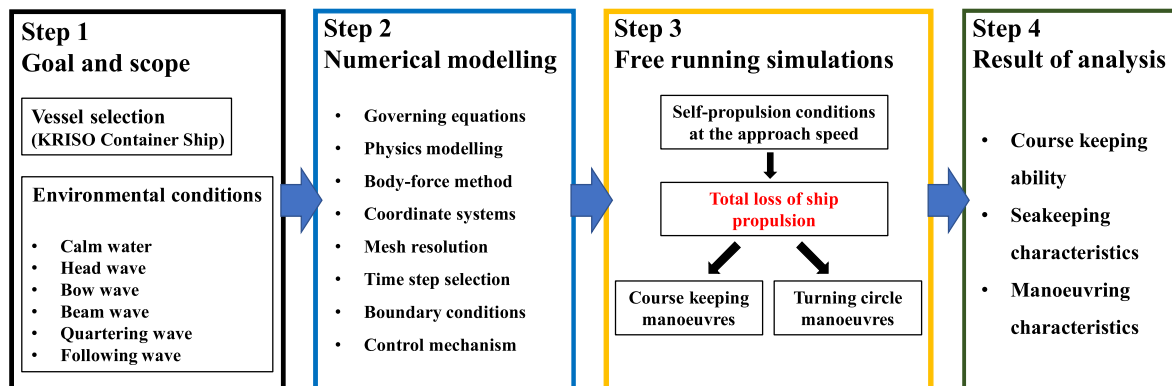


Fig. 2. Research methodology applied to the CFD free-running simulations.

**Table 1**

The principal particulars of the KCS model used in this study.

Main particulars	Symbols	Model scale (1:75.24)
Length between the perpendiculars	$L_{BP}(m)$	3.057
Length of waterline	$L_{WL}(m)$	3.0901
Beam at waterline	$B_{WL}(m)$	0.4280
Draft	$D(m)$	0.1435
Displacement	$\Delta(m^3)$	0.1222
Block coefficient	$C_B$	0.651
Ship wetted area with rudder	$s(m^2)$	1.6834
Longitudinal centre of buoyancy	% $L_{BP}$ , fwd+	-1.48
The metacentric height	$GM(m)$	0.008
Radius of gyration	$K_{xx}/B$	0.49
Radius of gyration	$K_{yy}/L_{BP}$ , $K_{zz}/L_{BP}$	0.25
Propeller diameter	$D_p(m)$	0.105
Propeller rotation direction (view from stern)		Right hand side
Rudder turn rate	(deg./s)	20.1

**Table 2**

The self-propulsion simulation cases to which the CFD model is applied prior to the course keeping and turning circle manoeuvres in the propulsion failure.

Case	Surge speed $U_0$ (m/s)	Propeller rev. (RPS)	Wave height $H$ (m)	Encounter Angle $\mu$ (degrees)	Encounter Period $T_e$ (s)	Froude Number $Fr$	Reynolds Number $Re$
1	1.094	13.38	Calm water	- (Calm sea)	—	0.200	$2.63 \times 10^6$
2	0.86	13.38	0.048	180 (Head sea)	1.004	0.157	$2.07 \times 10^6$
3	0.95	13.38	0.048	225 (Bow sea)	1.071	0.173	$2.29 \times 10^6$
4	1.07	13.38	0.048	270 (Beam sea)	1.399	0.195	$2.58 \times 10^6$
5	1.03	13.38	0.048	315 (Quartering sea)	2.103	0.188	$2.48 \times 10^6$
6	1.05	13.38	0.048	0 (Following sea)	2.694	0.192	$2.53 \times 10^6$

Successively, the course keeping (Fig. 3(a)) and standard turning manoeuvres (Fig. 3(b)) without propulsion power were carried out from the stable state of self-propulsion condition, respectively. Manoeuvrability restrictions as the consequence of propulsion loss can be identified by comparing the findings from this study with the manoeuvring results in normal operating conditions from Kim et al. (2021c).

## 2.2. Numerical modelling

In this study, the numerical computations of the free-running simulations were performed using the commercial CFD package STAR-CCM+, version 15.04. The details of the numerical modelling and computational schemes are described in this sub-section.

### 2.2.1. Governing equations

In the simulations, an Unsteady-Reynolds Navier-Stokes (URANS) method was adopted to solve the governing equations. The continuity and momentum equations can, for incompressible flows without body forces, be given in vectorial form as follows:

$$\nabla \cdot \mathbf{U} = 0 \quad (1)$$

$$\frac{\partial(\rho\mathbf{U})}{\partial t} + \nabla \cdot [\rho(\mathbf{U} - \mathbf{U}_g)\mathbf{U}] = -\nabla p + \nabla \cdot (\mu_{\text{eff}}\nabla\mathbf{U}) + \nabla\mathbf{U} \cdot \nabla\mu_{\text{eff}} + \mathbf{q}_i \quad (2)$$

in which  $\mathbf{U}$  is the fluid velocity and  $\mathbf{U}_g$  is the grid velocity;  $p$  is the static pressure;  $\rho$  is the fluid density;  $\mu_{\text{eff}} = \rho(\nu + \nu_t)$  indicates the effective dynamic viscosity, where  $\nu$  and  $\nu_t$  denote the kinematic and eddy viscosity, respectively ( $\nu_t$  is obtained from the turbulence model);  $\mathbf{q}_i$  is a user-defined source term.

In addition, the Volume of Fluid (VOF) method developed by Hirt and Nichols (1981) was adopted in the modelling of

multiphase flow of air and water. The transport equation can be written in Eq. (3) (Siemens, 2020):

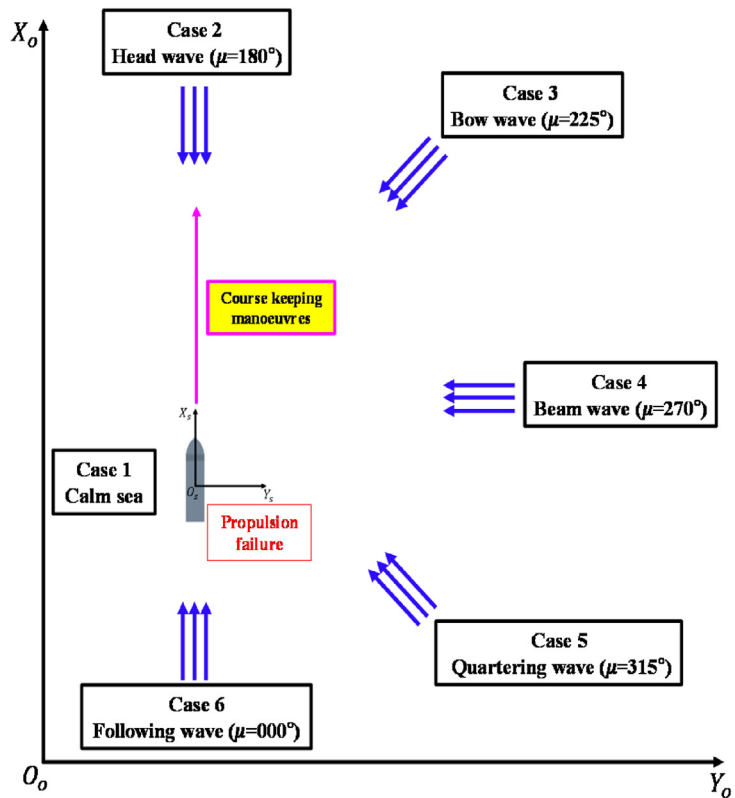
$$\frac{\partial\alpha_i}{\partial t} + \nabla \cdot [\alpha_i(\mathbf{U} - \mathbf{U}_g)] = S_{\alpha_i} - \frac{\alpha_i}{\rho_i} \frac{D\rho_i}{Dt} - \frac{1}{\rho_i} \nabla \cdot (\alpha_i \rho_i \mathbf{v}_{d,i}) \quad (3)$$

where  $\alpha_i$  is the volume fraction of phase  $i$  and this variable varies from 0 to 1 to describe the distribution as shown in Table 3;  $S_{\alpha_i}$  is a user-defined source term of phase  $i$ ;  $\frac{D\rho_i}{Dt}$  is the Lagrangian derivative of the phase densities  $\rho_i$ ;  $\mathbf{v}_{d,i}$  is the diffusion velocity. Undesired wave reflection can be mitigated by applying source terms for the momentum equation ( $\mathbf{q}_i$ ) and the VOF transport equation ( $S_{\alpha_i}$ ), as discussed in Perić and Abdel-Maksoud (2018).

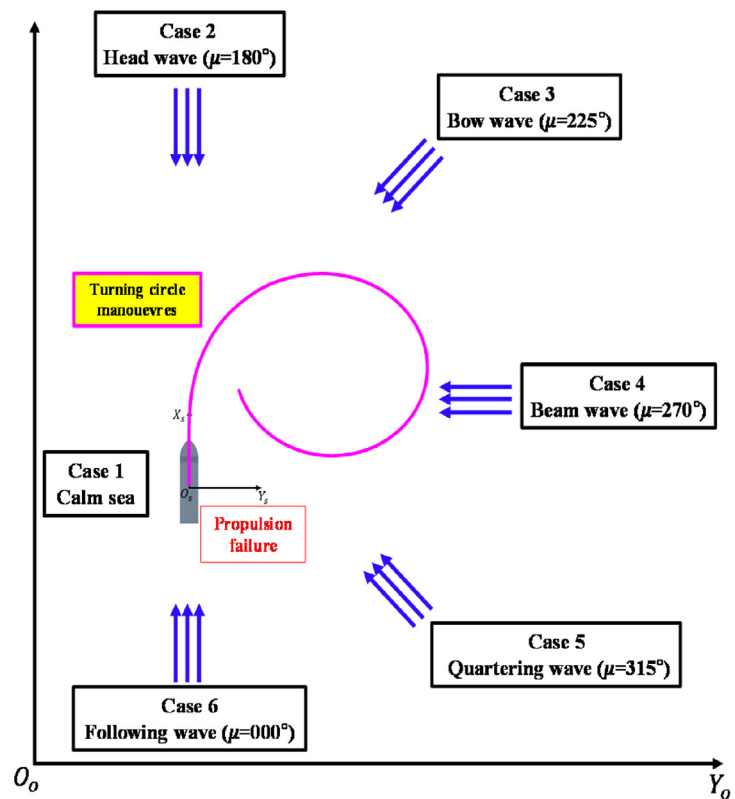
All computations were carried out using the RANS-VOF solver in STAR-CCM+. The solver employed uses a finite volume method which discretises the governing equations. A second order implicit backward Euler scheme was adopted for the temporal discretisation of the transient terms. The spatial discretisation is based on a second-order upwind scheme for the convection terms and a second-order centred scheme for the diffusive terms. SIMPLE (Semi-Implicit Method for Pressure-Linked Equations) was employed for the pressure-velocity coupling.

### 2.2.2. Physics modelling

The turbulence model chosen in this study was the Shear Stress Transport (SST) model (Menter, 1994). This model has been demonstrated to give accurate predictions of flows with adverse pressure gradients and flow separation, blending the best features of the  $k-\omega$  model in the near-wall region and the  $k-\epsilon$  model in the far-field. Menter's SST model has also been used in several previous works performed in the same area (Mofidi and Carrica, 2014; Wang et al., 2017; Wang and Wan, 2018; Kim et al., 2021a, 2021b, 2021c). Wall functions were applied to account for the viscous effects in the near wall boundary layer.



(a) Course-keeping



(b) Turning circle manoeuvres

Fig. 3. Schematic views of the simulation cases applied to this study, (a) course-keeping (b) turning circle manoeuvres.

**Table 3**  
vol fraction in a two-phase air-water flow.

Volume fraction	
Non-wetting phase (air)	$\alpha = 0$
Two-phase interface (free surface)	$0 < \alpha < 1$
Wetting phase (water)	$\alpha = 1$

The generation of non-linear regular waves in the free-running simulations was achieved by applying the fifth-order Stokes wave model which was proposed by Fenton (1985). A fifth-order wave is modelled with a fifth-order approximation to the Stokes theory of waves, which can more closely describe a realistic wave propagation than a first-order wave (Siemens, 2020). The wave profile and the wave phase velocity vary depending on the wave depth and wave height. It is of note that the VOF method has been used to great effect in modelling the Stokes regular waves by Tezdogan et al. (2015); Kim et al. (2021c).

### 2.2.3. Body-force propeller model

To simulate a ship propeller, the present CFD model applied the body force method which uses a body force momentum source model with an infinite-blade actuator disk. This method can model the flow field interaction between the hull, the propeller, and the rudder within an adequate level of accuracy while it offers a distinct advantage in terms of computational cost-benefit as stated in Kim et al. (2021c). According to Siemens (2020), the actuator disk model can be used for free-running manoeuvres by entering a number of input variables into the Star-CCM + software. For example, detailed information of the propeller performance curve, the rotational speed, the dimension and origin of the actuator disk, as well as the direction in which thrust is produced should be defined. As a result, the distribution of the axial and tangential forces of the modelled propeller and its effect on the flow is calculated. The integration of these forces over the disk yields the thrust and torque of the propeller, which are treated as body force terms in coupling with the DFBI module. The body force approach used in this work employed a uniform volume force  $\mathbf{f}_b$  distribution over the cylindrical actuator disk. It has to be pointed out that the volume force varies in radial direction, generating asymmetric flows. The radial distribution of the force components follows the Goldstein optimum and is expressed as follows:

$$f_{bx} = A_x r^* \sqrt{1 - r^*} \quad (4)$$

$$f_{b\theta} = A_\theta \frac{r^* \sqrt{1 - r^*}}{r^* (1 - r''_h) + r''_h} \quad (5)$$

$$r^* = \frac{r'' - r''_h}{1 - r''_h}, \quad r''_h = \frac{R_H}{R_P} \quad \text{and} \quad r'' = \frac{r}{R_P} \quad (6)$$

where  $f_{bx}$  represents the body force component in axial direction,  $f_{b\theta}$  represents the body force component in tangential direction,  $r$  is the radial coordinate,  $R_H$  is the hub radius and  $R_P$  is the propeller radius. The constants  $A_x$  and  $A_\theta$  are computed in the following equations, with  $T$ ,  $Q$ , and  $t_{disk}$  denoting the thrust, the torque, and the actuator disk thickness, respectively.

$$A_x = \frac{105}{8} \cdot \frac{T}{\pi t_{disk} (3R_H + 4R_P) (R_P - R_H)} \quad (7)$$

$$A_\theta = \frac{105}{8} \cdot \frac{Q}{\pi t_{disk} R_P (3R_H + 4R_P) (R_P - R_H)} \quad (8)$$

In this study, input parameters were chosen from the experimental information on the KCS propeller performed by Hiroshima University (SIMMAN, 2020).

### 2.2.4. Coordinate systems to solve 6 DOF motions

Four different coordinate systems were adopted for the free running model as presented in Kim et al. (2021c): (1) Earth-fixed coordinate ( $O_o - X_o Y_o Z_o$ ), (2) Ship-fixed coordinate ( $o_s - x_s y_s z_s$ ), (3) Propeller-fixed coordinate ( $o_p - x_p y_p z_p$ ), and (4) Rudder-fixed coordinate ( $o_r - x_r y_r z_r$ ). The earth-fixed coordinate is seen as an inertial frame to which has an origin fixed at point  $O_o$ . The ship's position and orientation are defined with respect to the earth fixed frame as three translations and three rotations. The ship-fixed coordinate system is a moving frame that rotates and translates in all 6-DOF with the ship. The origin  $o_s$  of the body-fixed system is located at the centre of mass of the ship. The axis  $o_s x_s$  is positive pointing to the bow, the axis  $o_s y_s$  is positive pointing to the starboard, and the axis  $o_s z_s$  is positive pointing downwards. The body-fixed frame is used to compute the hydrodynamic forces acting on the ship and to solve the governing equations of motion. The linear and angular velocities of the ship are described with respect to the body-fixed coordinate as the instantaneous body velocities. The linear and angular momentum equations in the ship-fixed coordinate system can be written as follows:

$$\begin{cases} X = m[\dot{u} + qw - rv] \\ Y = m[\dot{v} + ru - pw] \\ Z = m[\dot{w} + pv - qu] \end{cases} \quad (9)$$

$$\begin{cases} K = I_{xx}\dot{p} + (I_{zz} - I_{yy})rq \\ M = I_{yy}\dot{q} + (I_{xx} - I_{zz})pr \\ N = I_{zz}\dot{r} + (I_{yy} - I_{xx})pq \end{cases} \quad (10)$$

in which  $m$  is the mass of body  $u$ ,  $v$ ,  $w$  are the surge/sway/heave velocities  $p$ ,  $q$ ,  $r$  are the roll/pitch/yaw angular velocities  $X$ ,  $Y$ ,  $Z$  are the surge/sway/heave resultant forces acting on the ship  $K$ ,  $M$ ,  $N$  are the roll/pitch/yaw resultant moments acting on the ship  $I_{xx}$ ,  $I_{yy}$ ,  $I_{zz}$  are the moments of inertia about the principle axes in the body frame.

Unlike pure resistance or seakeeping simulations, propeller-fixed frame and rudder-fixed coordinate should be additionally defined in the manoeuvring simulations. The propeller-fixed coordinate is employed to specify the orientation of an actuator disk, i.e., the direction in which the disk produces thrust. In this frame, the positive  $x_p$ -axis points in the direction in which the rotating disk generates thrust force. The rudder-fixed coordinate is defined to introduce the axis about which the rudder blade rotates. The rudder rotates around the  $o_r z_r$  axis, which is controlled based on the prescribed manoeuvring mechanisms.

The use of the Dynamic Fluid Body Interaction (DFBI) method was applied with the aim of simulating the realistic motion of the ship during manoeuvring. The DFBI module enables the URANS solver to calculate the excitation forces and moments acting on the ship, and to solve the governing equations of rigid body motion to determine the new position and orientation of the ship (Siemens, 2020).

### 2.2.5. Mesh resolution

In the present study, meshes were generated using the built-in meshing capability of STAR-CCM+, which depends on the Cartesian cut-cell technique. The trimmed cell method was used to generate the volume meshes adequate for complex mesh problems, especially free-surface interactions. This method has been commonly used since it has the benefits of producing a high-quality grid, predominantly composed of unstructured hexahedral cells with trimmed cells next to the surface. The mesh density was adjusted using local surface and volumetric controls while a smooth transition of the grid was achieved by changing growth parameters to prevent interior, non-physical reflections. The surface grid was improved using a surface remeshing which presents a robust method of optimising the geometry surface for the volume meshes. To resolve the boundary layer region where high-velocity gradients were expected, six layers of orthogonal prismatic cells were generated using a prism layer mesher in combination with the trimmed cell mesher. The initial thickness of the prism layer was  $2.4 \times 10^{-5}$  m to reach a target  $y^+$  of 30. The mesh refinement was applied in each area of interest to resolve flow characteristics more accurately. The grids were refined in the free surface region for stable wave propagation. 20 grid points per wave height in the  $z$  direction and 80 grid points per wavelength in the  $x$  and  $y$  directions were generated according to the guidelines for ship CFD applications from ITTC (2011). It is worth noting that a constant cell size for both  $x$  and  $y$  directions was applied in the free surface refinement region to improve simulation stability, which proved to be effective by Romanowski et al. (2019). Additional refinements were included for the bow, the stern, the tight gap parts between the rudder blade and horn, and the propeller wake region. Two different grid generations were performed for each calm water and wave simulation, resulting in a computation mesh of approximately 5.4 and 7.2 million cells in total, respectively. The final computational mesh of the free-running ship model is illustrated in Fig. 4.

In order to handle the complex motions of the free-running ship model, the dynamic overset grid method was used in this study. This method provides great flexibility in modelling moving bodies compared to the rigid and deforming mesh motion options that may lead to cell quality problems. The overset mesh approach has the distinct advantages of enabling overset regions to move independently without any restrictions while ensuring a high-quality grid. As seen in Kim et al. (2021c), the computational domain with three different regions was designed for the present numerical model: 1) *background region*, 2) *hull overset region*, and 3) *rudder blade overset region*. The overlapping regions were generated in accordance with the hole-cutting process which couples the overset regions with the background region through the overset interfaces. Three types of cells are created from the hole-cutting process: 1) active cells, 2) inactive cells, 3) acceptor cells. The overset cell information regarding the present CFD model is displayed in Fig. 5 (donor cells are marked as active cells in another region). Siemens (2020) can be consulted for detailed information on the overset mesh technique. The background region enclosing the entire solution domain was generated to implement the far-field boundary conditions which determine the environmental conditions in our CFD simulations. The overlapping region which was tailored to the ship hull made it possible to simulate the full 6-DOF motions of the ship during manoeuvring. The rudder overset region was defined with the intention of enabling the rudder deflection based on the manoeuvring module. It should be noted that the distance of the gap part between the rudder and rudder

root was adjusted to obtain valid interpolations between the grids. A linear interpolation scheme was used to link solutions between two overlapping grids.

### 2.2.6. Determination of the time step

The time step can be determined to satisfy the Courant number (CFL) condition or to resolve the flow characteristics of interest. In implicit unsteady simulations, the time step is generally chosen by the flow features rather than the CFL condition. ITTC (2011) recommends that at least 100 time steps per encounter period should be used for the regular wave simulation. In this study, the time step was set at  $5 \times 10^{-3}$  s. This figure is more than twice smaller than that calculated from the recommendation put forward by ITTC (2011). This ensures the accuracy and reliability of the simulation results.

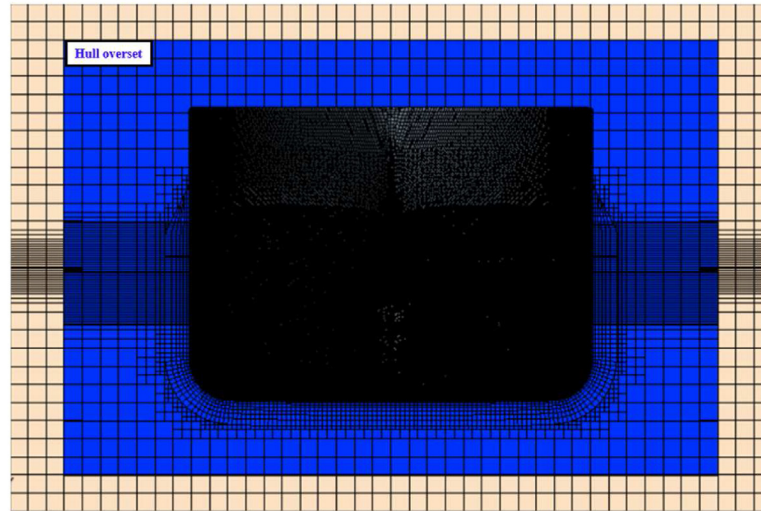
### 2.2.7. Computational domain and boundary conditions

In the CFD simulations, the determination of appropriate boundary conditions is crucial in order to achieve reliable results and reduce unnecessary computational costs. Fig. 6 illustrates the computational domain with the imposed boundary conditions and the dimensions of the domain. For the opposite faces in the  $x$ -direction, a velocity inlet boundary condition was applied. The side walls and bottom wall were set as a velocity inlet while the top boundary was modelled as a pressure outlet condition to represent an open sea, which means deep water and infinite air conditions. The ship hull and the rudder blade were defined as no-slip wall boundary conditions. To prevent wave reflection from the boundaries, the VOF wave damping capability of the software package was used for the calm water simulation, whereas the wave simulations adopted the wave forcing capability. With the aim of preventing wave reflection from the boundaries, the VOF wave damping capability of the software package was employed for the calm water simulation, whereas the wave forcing capability was used for the wave simulation. Both the damping and the forcing modules were applied at all the vertical boundaries (the up-and-down stream boundaries and side walls) with a damping/forcing length equal to  $1.0 L_{BP}$  ( $\sim 3.06$  m).

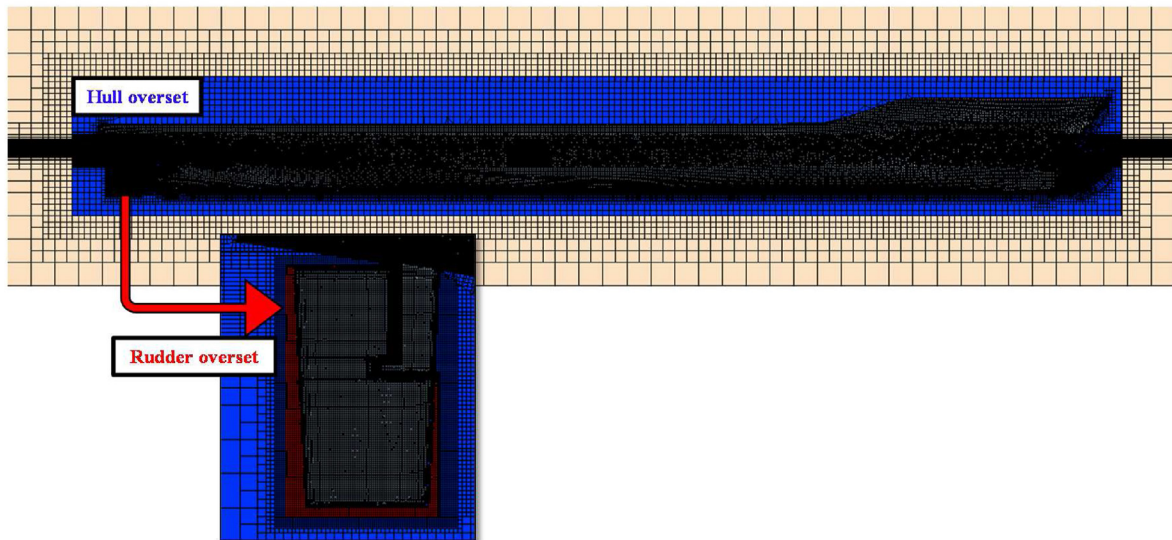
As previously mentioned, the present CFD model was composed of three different regions, i.e., one background region and two overset regions. Each computational region adopted different motion capabilities with a hierarchy of bodies for the free-running simulations. Firstly, the motion of the hull overset region (parent body) was defined as the DFBI rotation and translation module, which enables the ship to move in all degrees of freedom. Secondly, the rudder overset region (child 1) was set to be a child of the ship hull, and thus followed the ship during manoeuvring, while the rudder deflection was controlled based on the manoeuvring mechanism. In the same manner, the motion of the actuator disk (child 2) was defined to follow the ship, and its revolution was adjusted according to a propeller controller. Lastly, the background region was forced to follow the horizontal motion of the ship (surge, sway, and yaw) to guarantee the desired free surface.

### 2.2.8. Control mechanism

Two different types of free-running manoeuvres were performed to evaluate the effect of the propulsion loss on the ship's manoeuvrability: *course keeping control* and *turning circle manoeuvre*. Prior to the start of the free-running manoeuvres under the propulsion failure condition, the self-propulsion computation was first carried out for the propeller revolution of 13.38 RPS with



a) Midship cross-section of the domain



b) Profile view cross-section of the domain

Fig. 4. Mesh structure of the computational domain.

the ship free to move in full 6DOF motion. After the target surge speed was reached, the revolution speed of the actuator disk was compelled to change suddenly according to the propeller control module. This was introduced to represent the failure condition of the ship propulsion system, which is presented by the following expression:

$$n(t) = \begin{cases} n_s & (t < t_f) \\ 0 & (t \geq t_f) \end{cases} \quad (11)$$

where  $n(t)$  is the revolution rate of the actuator disk (RPS) at a given time,  $n_s$  is the revolution rate at the self-propulsion point (13.38 RPS in this work), and  $t_f$  indicates the time when the propulsion failure started.

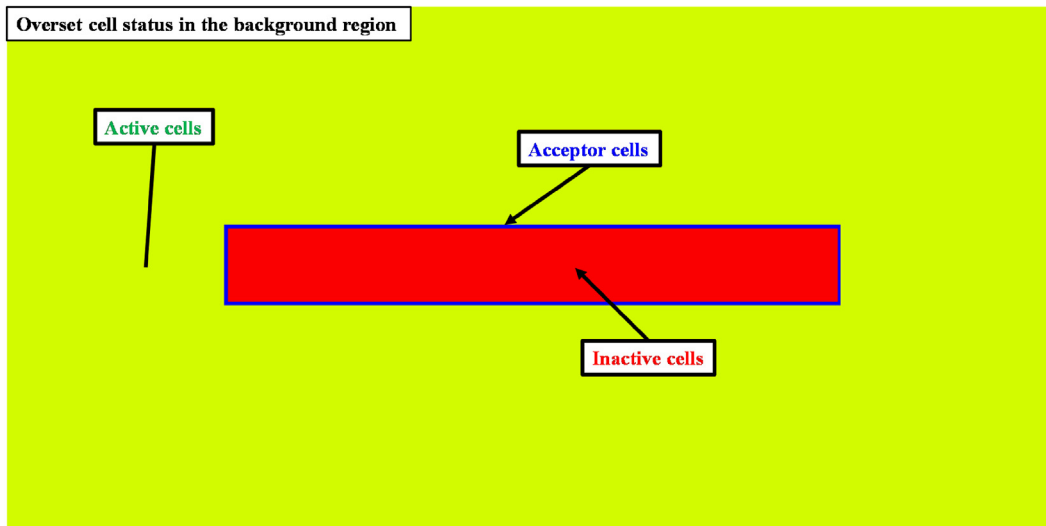
Subsequently, after the propulsion failure condition was achieved, the ship manoeuvring performance was evaluated by the course keeping control and turning circle manoeuvres, respectively.

During the course keeping control, the rudder angle was controlled by the Proportional-Integral-Derivative (PID) feedback controller. The control function is expressed as follows:

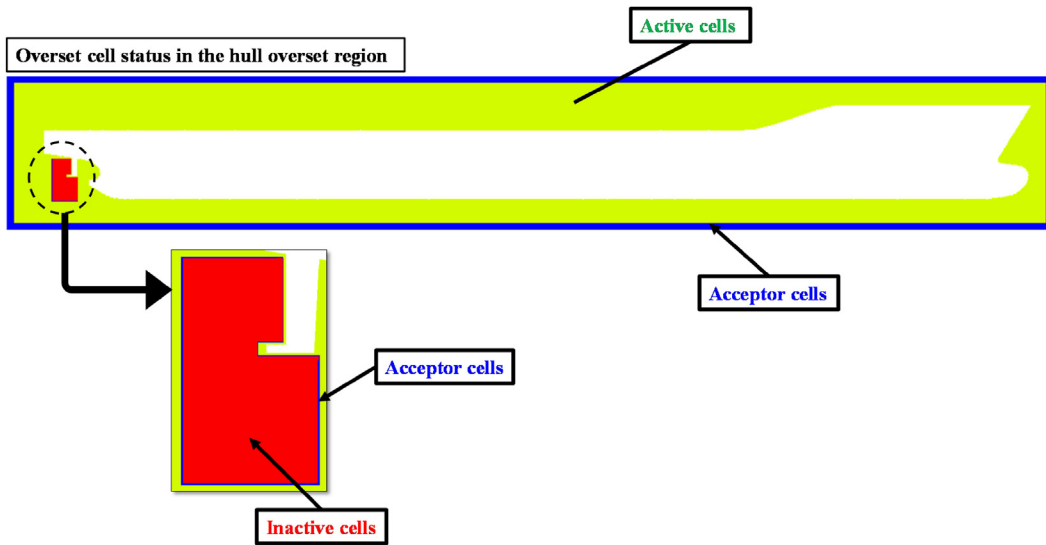
$$\delta(t) = K_p e(t) + K_i \int_0^t e(t) dt + K_d \frac{de(t)}{dt} \quad (12)$$

$$e(t) = \psi(t) - \psi_c \quad (13)$$

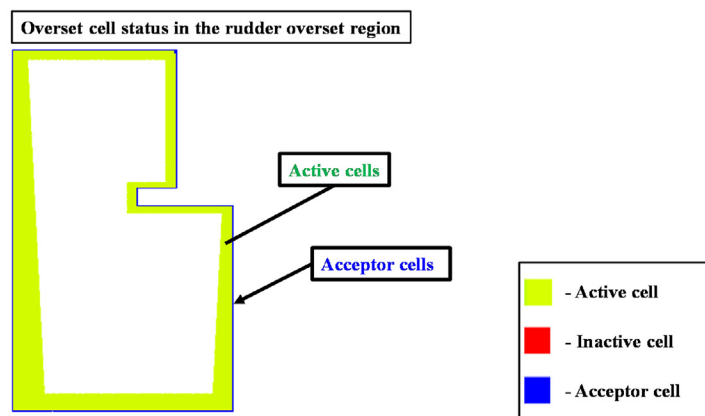
in which  $\delta(t)$  means the rudder angle,  $\psi(t)$  the instantaneous yaw angle at a given time, and  $\psi_c$  the target yaw angle.  $K_p$ ,  $K_i$ , and  $K_d$  indicate the proportional, integral, and derivative control gains, respectively. Throughout all the simulations, the control gains were determined at  $K_p = 5$ ,  $K_i = 0.05$ , and  $K_d = 3$  after several trials and errors. The target yaw angle ( $\psi_c$ ) was selected at  $0^\circ$  to make the ship advance straight in calm water or in waves. It should be noted that the optimal control gains of the PID controller can be adjusted



(a) Overset cell status in the background region



(b) Overset cell status in the hull overset region



(c) Overset cell status in the rudder overset region

Fig. 5. Overset cell status in each region.

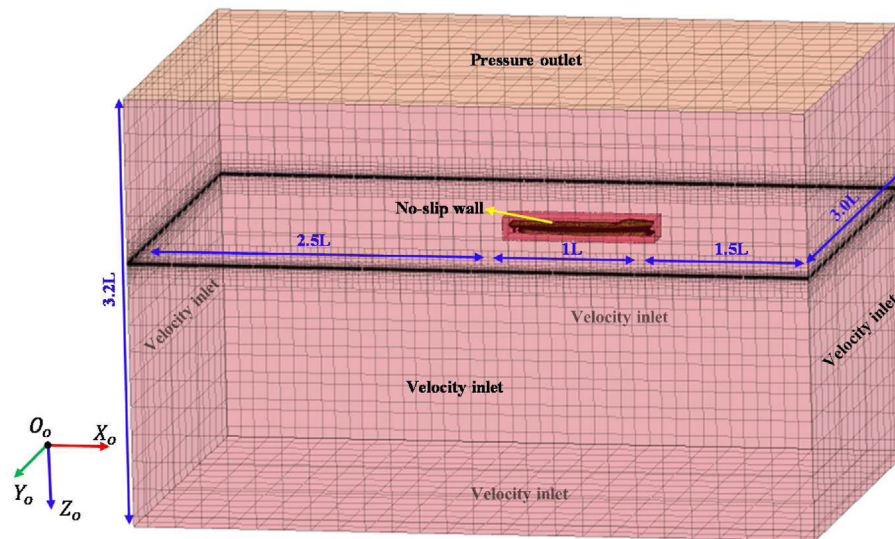


Fig. 6. The computational domain with the imposed boundary conditions.

depending on environmental disturbances.

On the other hand, the open loop controller was designed to perform the standard turning circle manoeuvre. The control mechanism is given as follows:

$$\delta(t) = \begin{cases} \max(0, kt), & \delta \leq 35^\circ \\ 35^\circ & \end{cases} \quad (14)$$

with  $k$  indicating the maximum rudder rate. The maximum rudder rate was set to be  $k = 20.1^\circ/\text{s}$  which follows the setup of experimental tests (Yasukawa et al., 2021). As indicated by the definitions above, the turning circle manoeuvre turns the rudder blade to  $35^\circ$  which is kept constant until the turning simulation ends.

The free-running manoeuvres proposed in this sub-section were applied to the KCS model to estimate the effects of the propulsion loss on the manoeuvring behaviour. The comparison of the results from this study to those with the normal operating condition in the literature (Kim et al., 2021c) was made with a view to identifying the changes in the ship's manoeuvrability under the failure of the propulsion system. For each manoeuvring simulation, 13440 CPU hours with 40 CPU processors were needed, completed in approximately 336 wall clock hours.

### 3. Case studies

#### 3.1. Verification and validation study

In general, the numerical uncertainties of CFD models can be quantified by a verification study (i.e. spatial convergence study and temporal convergence study). In this study, however, a verification study has not been conducted due to the high computational cost involved in simulating the free-running manoeuvres. It is worth noting that a verification study has rarely been carried out for free-running simulations by other researchers in this field (Mofidi and Carrica, 2014; Wang and Wan, 2018; Liu et al., 2020). In addition to the computational cost, verification studies may be hampered by the fact that the grid refinement and coarsening for the overset regions (especially for the overlapping region around the rudder) are also highly demanding, as stated in Mofidi and Carrica (2014). Fortunately, Kim et al. (2021c) performed a series of spatial and temporal uncertainty studies for similar manoeuvring problems

using the same CFD model and an acceptable convergence level was achieved. According to Kim et al. (2021c), CFD uncertainties for important manoeuvring parameters such as the advance, transfer, and tactical diameter were calculated to be a maximum of 0.28% in the grid sensitivity study and 0.19% in the time-step sensitivity study using the grid convergence index method.

The open water characteristics of the infinite actuator disk were estimated before performing the self-propulsion computations. The open water simulation was carried out for the same conditions as the experimental ones with a wide range of advance coefficients  $J$  varying from 0.05 to 0.95. Thrust coefficients  $K_T$ , torque coefficients  $K_Q$ , and efficiency  $\eta_0$  for each advance ratio  $J$  were calculated from the predicted thrust and torque. As reported in the authors' previous work (Kim et al., 2021c), the results showed that both the thrust and the torque were slightly overpredicted as the propeller load decreased ( $J \geq 0.4$ ), whereas they were underpredicted at a higher load ( $J < 0.4$ ). The expected self-propulsion point of the KCS ranged from  $J = 0.4$  to  $J = 0.6$ , where the predicted thrust and torque showed excellent agreement with the experiments with errors up to 1.6%, as shown in Kim et al. (2021c). This indicates that the actuator disk based on the body force method can predict the open-water curves regarding the thrust and torque. Throughout all the CFD simulations in this study, the self-propulsion conditions were achieved using this actuator disk model. When the ship lost its propulsive power, in practice, a stopped propeller is expected to impose a drag load on the ship hull. However, this effect was not taken into account in this paper due to the use of the actuator disk and may affect the accuracy of the simulations.

Unfortunately, the experimental results for the KCS's manoeuvring performance under the propulsion failure condition are not available in the literature and hence a comparison could not be made. However, the manoeuvring behaviour of the KCS in both calm water and head waves has been extensively validated in the authors' previous work (Kim et al., 2021c) using the present free-running model. According to their results, the predicted ship motions, critical manoeuvring indices, and other hydrodynamic features were reasonably consistent with the experimental results. The present CFD model can thus be claimed to be validated and is sufficiently reliable for predicting the manoeuvring performance of the ship in question. This model was therefore used to estimate the

ship's manoeuvrability under the propulsion loss condition, as coupled with the propeller control module.

### 3.2. Course keeping control

This section will present the manoeuvring performance of the KCS experiencing the propulsion failure during the course-keeping in both calm water and waves.

As stated previously, the self-propulsion conditions in calm water and waves were initially achieved to reach the target surge speed before the course-keeping control. Fig. 7 presents the time histories of the ship speed, ship motions, and various hydrodynamic quantities during the course-keeping control for all cases. From the graphs given in the figure, the values on the dotted lines mean the normal operating condition where the ship was moving forward with the propeller rotational speed of 13.38 RPS ( $0 < t < 10$ ). The values on the solid lines indicate the propulsion loss condition in which the propeller speed was set at zero in order to represent the failure of the ship propulsion system ( $10 = t$ ).

As for the surge velocity, it was found to vary depending on the wave propagation direction under the same propeller revolution ( $0 < t < 10$ ). This is because the different pressure distribution around the ship hull was caused according to the wave direction, which led to differences in the added resistance in the sailing direction. The surge speed started to decrease after the ship lost its propulsion power ( $10 = t$ ) as expected, while the ship resistance also followed the same trend. The speed loss rate between the initial surge speed and the minimum value was predicted at 63% for

the calm sea, 79% for the head sea, 70% for the bow sea, 63% for the beam sea, 61% for the quartering sea, and 69% for the following sea within the same period ( $10 = t \leq 56$ ). The ship experienced a large reduction in the surge velocity when sailing forward in the head and bow waves, which implies that the waves coming from the ship's bow caused a greater resistance than the other wave headings.

The propulsion failure was also observed to have a great influence on the ship motions under course keeping control. For the heave and pitch motions, the wave-encounter frequency was identified as the key factor leading to significant changes in such motions. The time histories of the encounter frequencies during the course-keeping in waves are displayed in Fig. 8, where the natural frequencies of the pitching, heaving and rolling system are also indicated. It can be seen from the figure that after the propulsion failure, the ship experienced substantial changes in the encounter frequency of the wave except for Case 4 (the beam wave). Such changes resulted from continual changes in the surge speed as well as the heading angle (i.e., the ship's heading angle relative to the wave direction). It is of note that the maximum heave and pitch motions occur when the encounter frequency ( $f_e$ ) equals, or is close to, the natural frequency of the heaving and pitching motions ( $f_n$ ). For the KCS model, the natural frequencies of the heaving and pitching system are close to  $f_n \approx 0.93$  Hz in which the maximum excitation force is expected to occur, as shown in Kim et al. (2021c). The greater the difference between the encounter frequency ( $f_e$ ) and the natural frequency ( $f_n$ ), the smaller the excitation force can be, causing the decrease in the amplitude of the heave and pitch

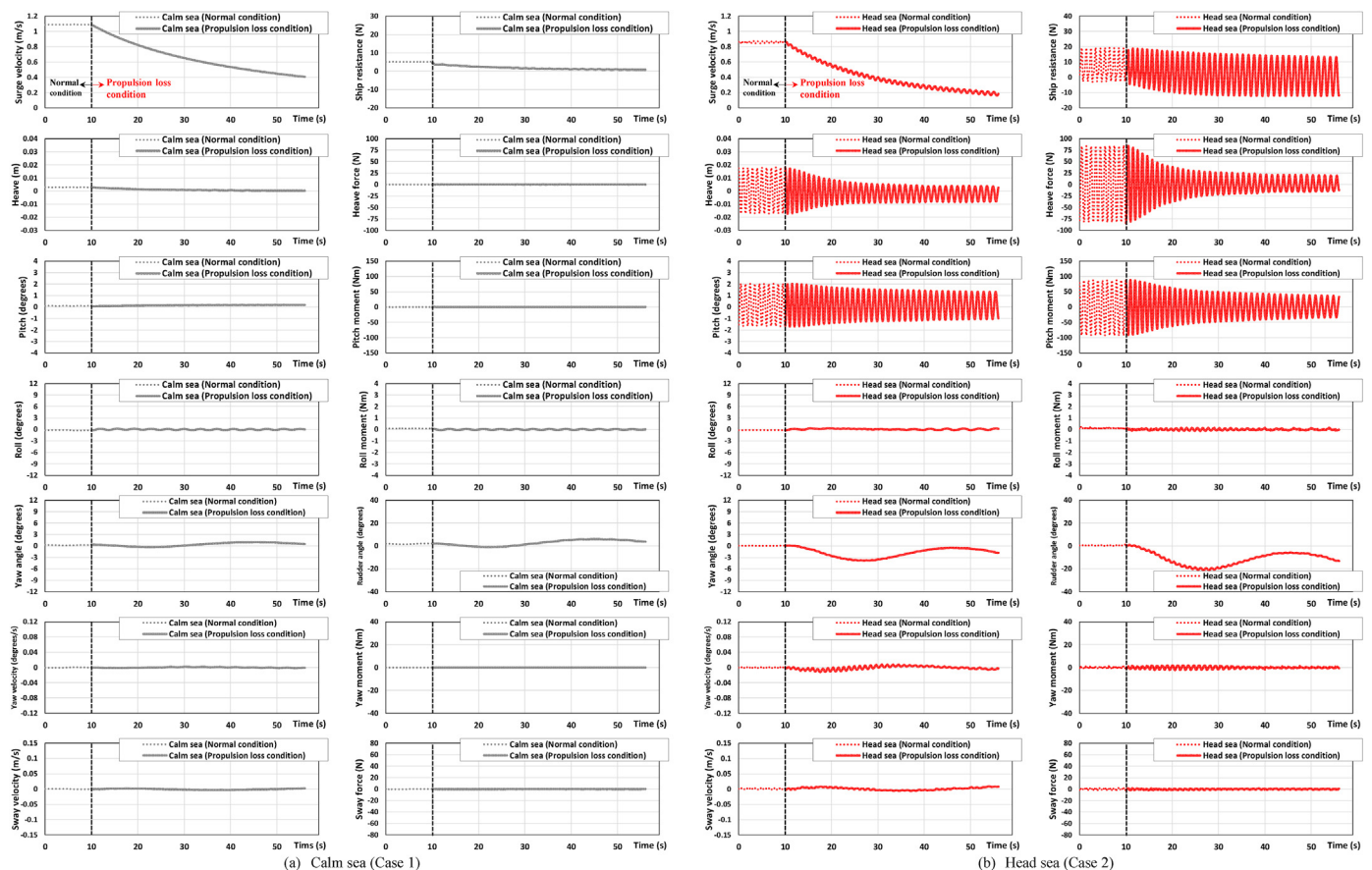


Fig. 7. The time histories of the ship speed, ship motions, and various hydrodynamic quantities during course keeping control.

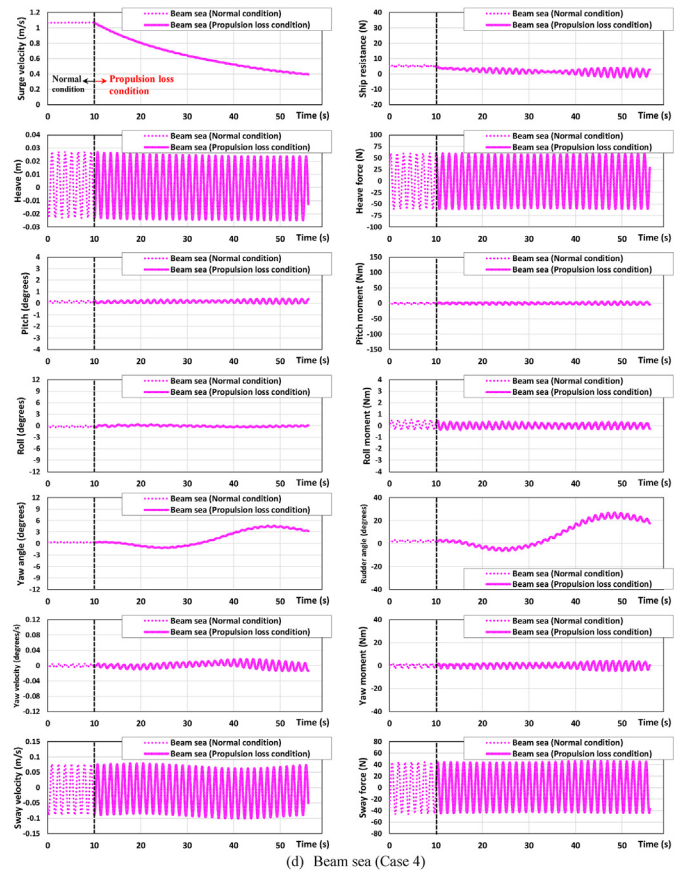
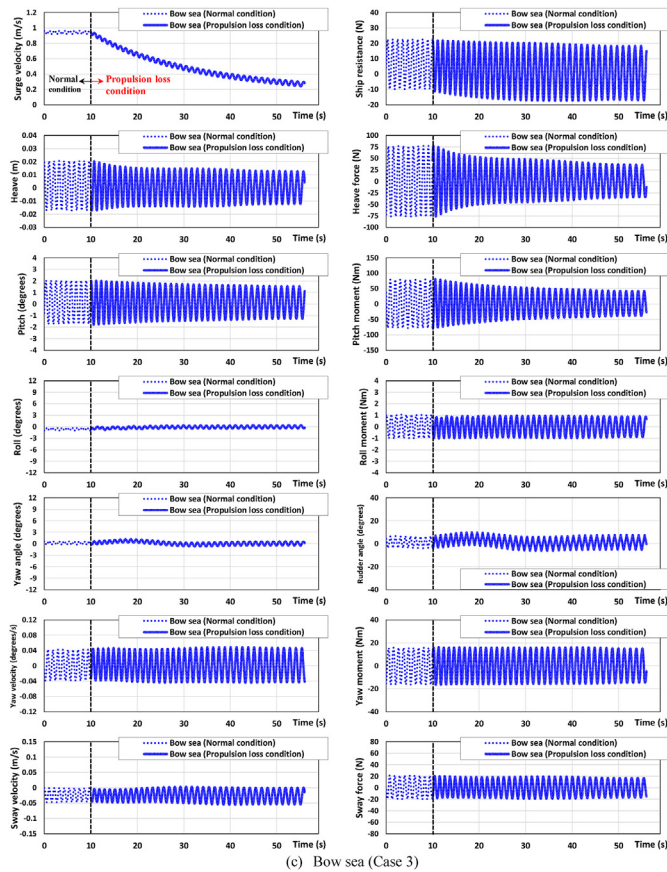


Fig. 7. (continued).

motions. In this study, Case 2 (the head wave) and Case 3 (the bow wave) in the normal condition have frequencies of encounter of 0.995 Hz and 0.933 Hz, respectively, both very close to the natural heave and pitch frequencies. When the ship was moving forward in the head or bow waves under the propulsion loss condition, the wave-encounter frequency decreased with the decrease in the surge speed. The decrease of the wave encountering frequency led to an increase in the difference between the encounter frequency and the natural frequency, causing a decrease in the excitation force. Consequently, this caused the heaving and pitching amplitude to decrease, as shown in Fig. 7(b)–(c). When the ship was sailing in the quartering and following waves (Fig. 7(e)–(f)), on the other hand, it was predicted that the amplitude of the heave and pitch motions slightly increased with the decrease in the surge speed. This is due to the fact that the encounter frequency in such wave conditions becomes slightly close to the natural frequency of the heave and pitch motions as the surge speed decreased. Interestingly, the heave and pitch responses in the beam wave case were almost kept constant since the wave coming from the beam did not change the wave-encounter frequency even though the surge speed of the ship decreased. The heave and pitch motions in calm water (Fig. 7(a)) were found to be negligible both under the normal condition and the propulsion failure condition due to the absence of external loads. As for the roll motion, the large amplitude of the roll angle was predicted in the quartering wave condition (Case 5) during the course-keeping compared to the other cases. The possible reason for this could be that the rudder deflection angle

became comparatively large in the quartering seas right after the propulsion failure, which may lead to the significant rudder normal force and thus cause the relatively large roll motion.

In general, ships sail to their destination ports based on the planned navigation route which is determined before the start of the voyage from berth to berth. When planning the route, navigation officers take into consideration a series of safety factors associated with route characteristics to ensure safe navigation at sea. Thus, ships need to follow the planned route to avoid unidentified hazards which could lead to navigational casualties. However, ships advancing in a real seaway experience deviations from the planned course because of the presence of external disturbances, which indicates the poor performance of the course keeping control. In particular, the course keeping capability of a ship is predicted to deteriorate as a result of the propulsion system failure. This can pose a serious threat to the safe operation of a ship, increasing the likelihood of encountering unknown hazards such as navigation obstacles or shallow water which could lead to navigational casualties (collision and grounding). Therefore, it is necessary to understand the course keeping behaviour of a ship in a real sea state under the propulsion loss for making proper decisions regarding ship-handling actions.

The time histories of different variables related to the course keeping ability for each simulation are also presented in Fig. 7: yaw angle, rudder deflection angle, yaw velocity, yaw moment, sway velocity, and sway force. It was identified that the ship's heading control was more challenging in the propulsion loss condition than

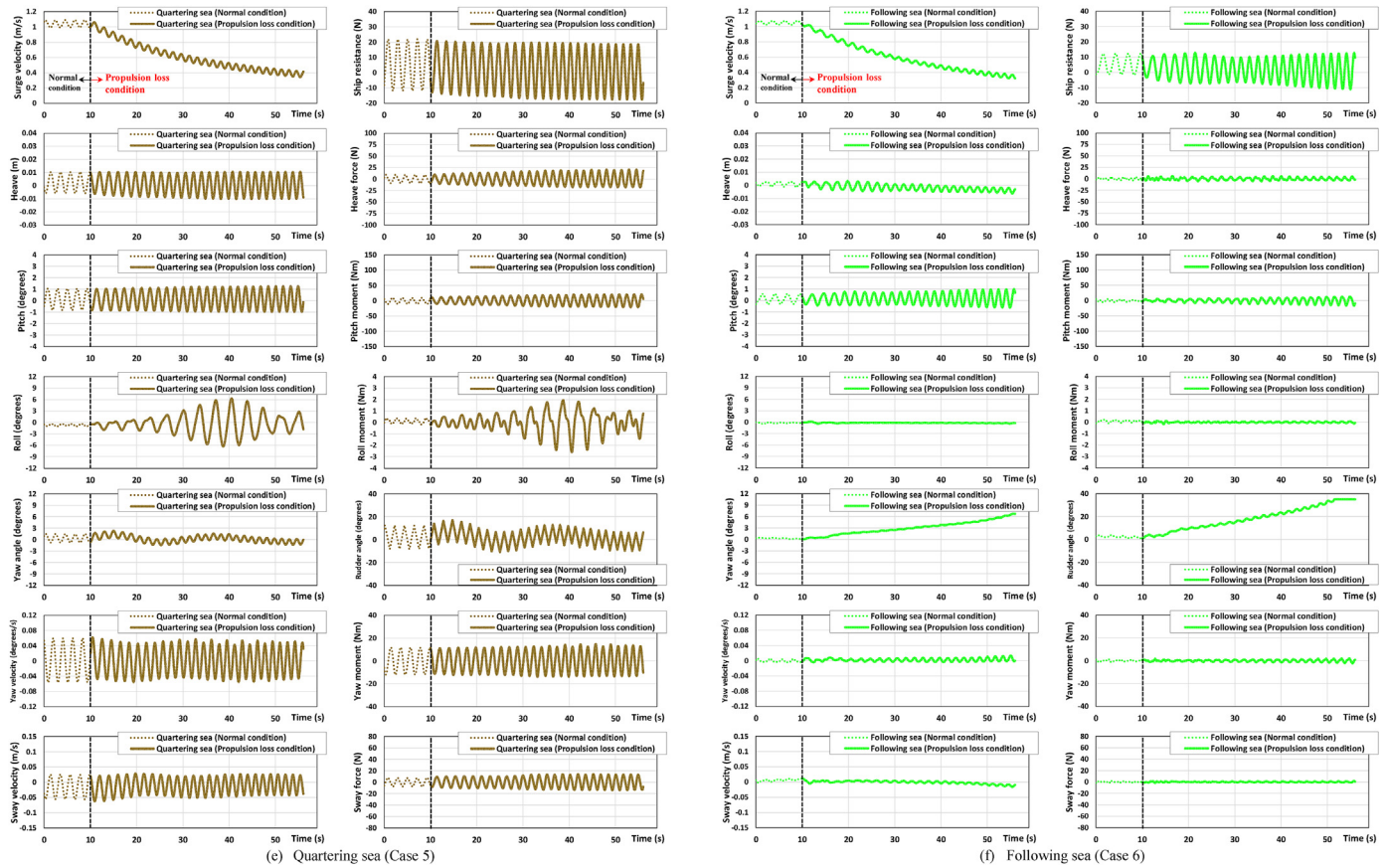


Fig. 7. (continued).

in the normal condition, such that the rudder deflection became larger after the ship lost its propulsion power. This is because the inflow velocity to the rudder was significantly reduced after the propulsion failure, thus causing the rudder normal force to decrease. The ship's heading control in calm water was not an issue under the propulsion loss because there were no external environmental loads. With the aim of visualisation, Fig. 9 shows the snapshots of the axial flow velocities around the rudder and the pressure distributions on the rudder in the calm water condition. The pictures are the snapshots from the simulation of Case 1 (the calm water case and normal operating condition). When the ship was advancing forward in calm water, the pressure difference between the starboard and the port of the rudder blade was formed due to a non-uniform flow created by the actuator disk. This caused a small rudder lift, and thus the yaw moment to turn the ship to the starboard to a small extent. However, the wave conditions showed different responses in terms of the course keeping control under the propulsion loss. The relatively large deviations of the yaw angle were estimated in the head, beam, and following sea conditions with the large rudder deflections. This stemmed from not only the reduced rudder normal force but also the uneven pressure distributions on the hull caused by the incident wave, generating a yaw moment to change the ship's heading. Interestingly, the oblique wave conditions, namely the bow and quartering seas, showed relatively small changes in the yaw angle within a value of  $2^\circ$  during the manoeuvre. Such small changes in the ship's heading may be closely associated with the pressure distribution on the ship hull caused by the propagating oblique waves.

A comparison of the predicted ship trajectories during the course-keeping for each case is displayed in Fig. 10, where dotted

lines represent the ship paths in the normal conditions and solid lines indicate ones in the propulsion loss condition. This clearly illustrates the influence of the propulsion system failure on the course keeping behaviour of the ship. As can be seen from the figure the ship under propulsion loss condition experienced unexpected changes in the ship trajectory compared to the normal condition. Such course keeping behaviours resulted from the yaw motion after the ship lost its propulsion power, and the resultant yaw motion is closely associated with the presence of external disturbances as well as the rudder behaviour determined by the PID controller. After the propulsion loss, the ship sailing in calm water experienced the smallest change in the trajectory during the manoeuvre, which indicates the good performance of the course keeping control in calm water. This may be due to the absence of external disturbances which cause lateral forces and yaw moments on the ship. It was found that the following sea condition led to the largest change in the path. This can be explained by the fact that the predicted yaw motion of the ship shown in Fig. 7(f) consecutively kept positive values (the starboard turning), which made the ship continue to move to the starboard side. Despite the successful control of the yaw angle, the ship advancing forward in the bow sea experienced a large change in the course because of the wave drift forces and moments. The drift direction of the ship trajectory was estimated to be similar to the wave propagation direction ( $\mu = 225^\circ$ ). Another reason for the large change in the trajectory was found to be the decreasing surge speed as the ship advanced, which strengthened the effect of the wave drift force on the ship's path. For the rest of the cases (the head, beam, quartering seas), the trajectory changes were noted to some extent due to the wave drift force and the changes in the ship's heading angle. It has to be noted

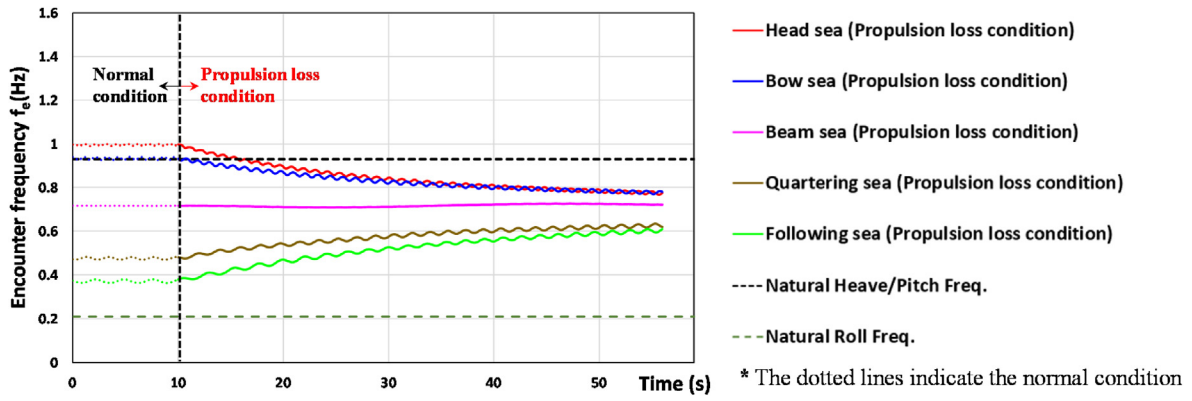


Fig. 8. The time histories of the encounter frequencies during the course-keeping in waves.

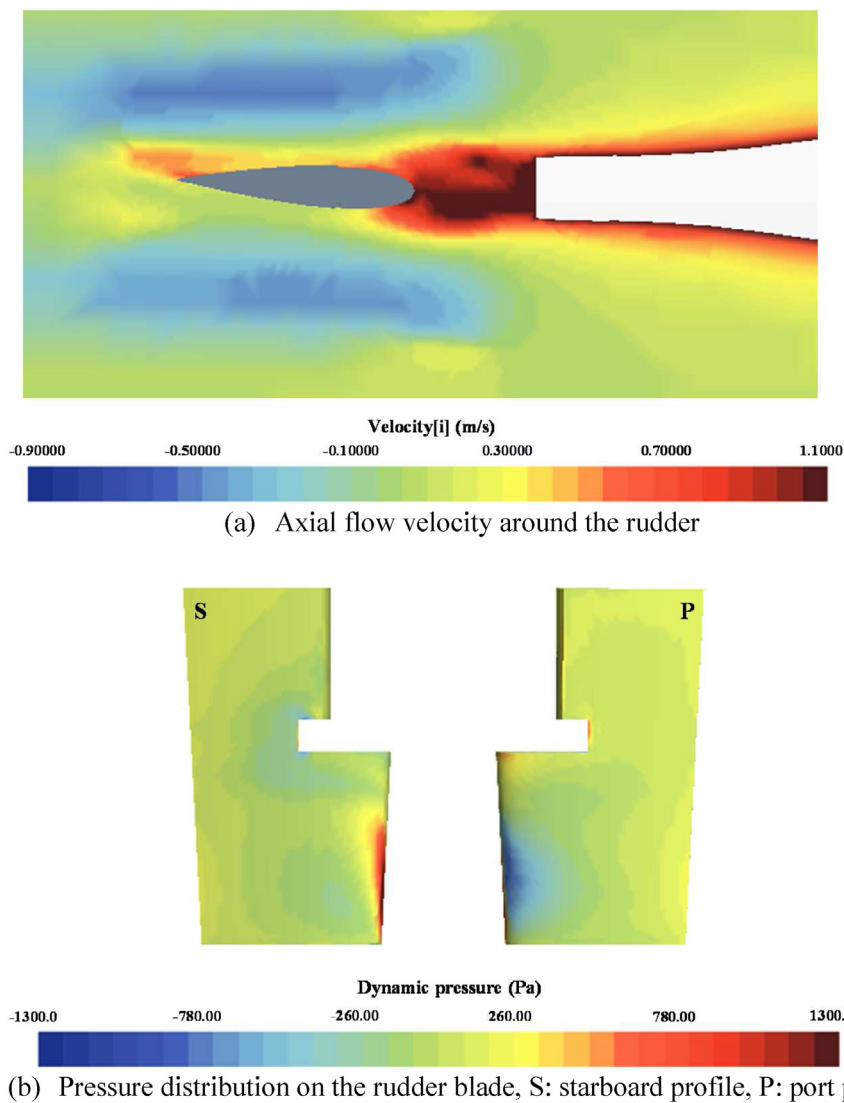


Fig. 9. The snapshots of the axial flow velocities around the rudder and the pressure distributions on the rudder under the course-keeping in the calm water condition (normal operating condition).

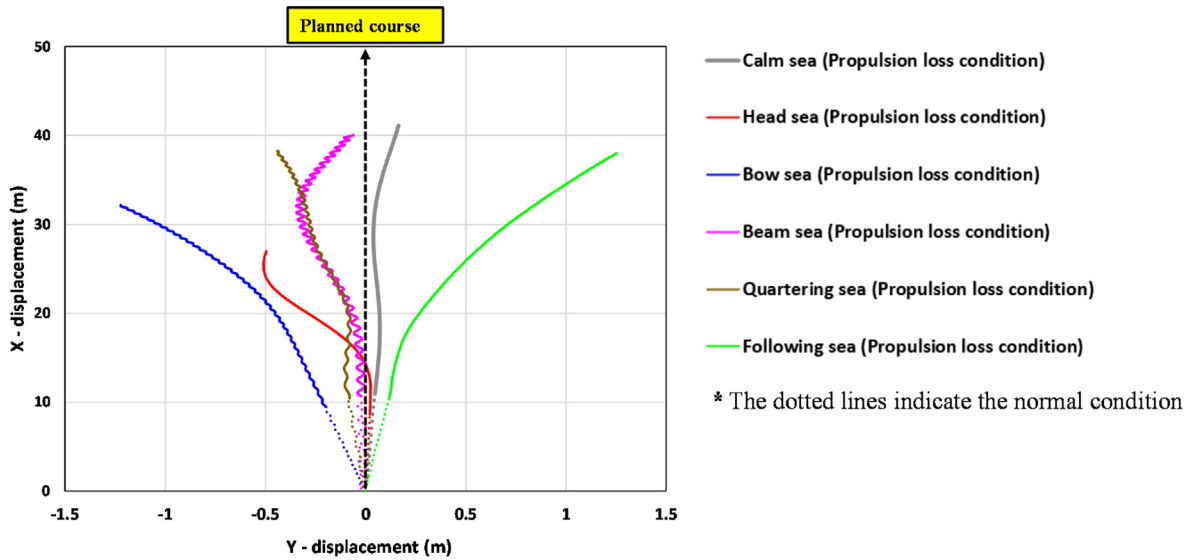


Fig. 10. The comparison of the predicted trajectories for all the cases.

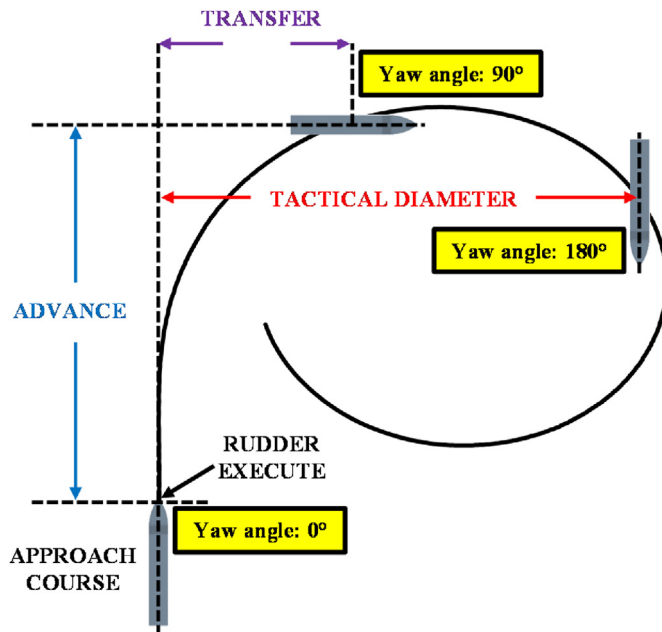


Fig. 11. The definitions of turning parameters.

that the ship trajectory could be less deviated from the straight course with different PID gains or by manual steering in real navigation operations. The relatively large oscillations of the ship paths were found under the beam and oblique waves, which was closely related to the sway forces acting on the ship, as shown in Fig. 10.

### 3.3. Turning circle manoeuvre

This section will discuss the effects of the propulsion failure on the ship's turning manoeuvre by comparing the critical manoeuvring parameters between the normal condition and the propulsion loss condition. These manoeuvring quantities have been

identified by ITTC (2021), as shown in Fig. 11. The details of the ship's manoeuvrability in the normal operating condition can be found in Kim et al. (2021c).

All the predicted trajectories of the turning circle manoeuvre under both the normal and propulsion loss conditions are presented in Fig. 12. The starting points of the turning manoeuvre were shifted to the specific location (0,0) for the correct comparisons of the trajectories. For each case, the simulations of both conditions (the normal and propulsion failure conditions) were run for the same simulation duration so that the impacts of the propulsion loss on the ship's manoeuvrability are comparable. It should be noted that the simulations in the normal condition were completed when the heading angle variation up to 360° was achieved. Table 4 provides the manoeuvring indices and hydrodynamic loads acting on the rudder and hull in the normal and the propulsion failure conditions, each identified by their case numbers (peak values during the initial phase of the turn and mean values during the steady phase of the turn).

The critical turning parameters are highly dependent on the ship's horizontal motions, namely surge, sway, and yaw motions which are determined by the complex interactions between the hull, propeller, rudder, and environmental loads. Such ship motions have a close correlation with the ship velocities in the horizontal plane (surge, sway, and yaw velocities). In general, the greater the surge speed and the smaller the yaw velocity, the greater the ship advance and transfer can be, as discussed in Kim et al. (2021c). For all the cases, it was identified from the figure and the table that the turning capability of the ship was strongly affected by the presence or absence of the propulsion power, thus leading to substantial changes in the turning trajectories. The propulsion loss condition led to notable increases in the advance, the transfer, and the time to turn by 90°, as seen in Table 4. This is mainly due to the loss of propulsion power, which caused the decrease in the rudder inflow velocity. Hence, the sufficient rudder normal force was not achieved and thus leading to the longer time to turn by 90°. As a result of this, the ship advance and transfer for the propulsion loss condition were found to be comparatively large despite the small surge speed. The resultant differences in the turning trajectories between

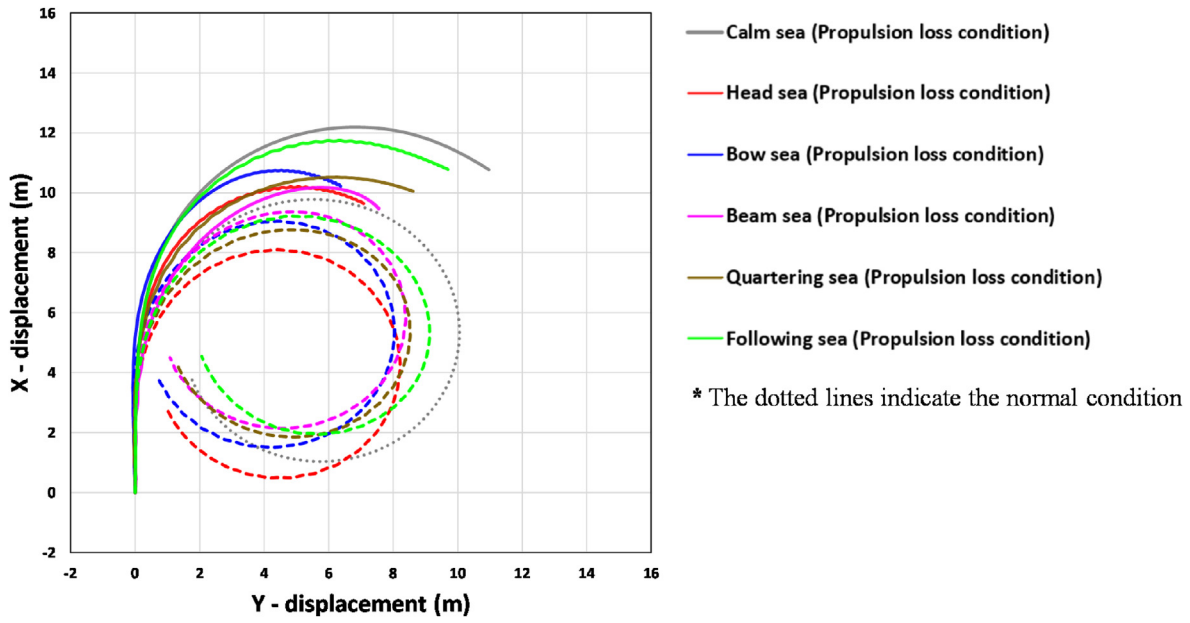


Fig. 12. The turning circle trajectories in both normal condition and propulsion loss condition.

Table 4

CFD results: turning indices and hydrodynamic loads in the normal operating and propulsion failure conditions.

Parameters (CFD results)	Calm sea (Case1)	Head sea (Case 2)	Bow sea (Case 3)	Beam sea (Case 4)	Quartering sea (Case 5)	Following sea (Case 6)
<b>Normal operating conditions</b>						
Advance (m)	9.55 (3.13 L <sub>BP</sub> )	7.86 (2.57 L <sub>BP</sub> )	8.85 (2.90 L <sub>BP</sub> )	9.10 (2.98 L <sub>BP</sub> )	8.44 (2.76 L <sub>BP</sub> )	8.95 (2.81 L <sub>BP</sub> )
Transfer (m)	4.07 (1.33 L <sub>BP</sub> )	3.09 (1.01 L <sub>BP</sub> )	3.10 (1.01 L <sub>BP</sub> )	3.43 (1.12 L <sub>BP</sub> )	3.25 (1.06 L <sub>BP</sub> )	3.56 (1.16 L <sub>BP</sub> )
Time for yaw 90° (s)	12.31	12.52	13.09	11.92	11.23	11.76
Tactical diameter (m)	9.82 (3.21 L <sub>BP</sub> )	7.97 (2.61 L <sub>BP</sub> )	7.82 (2.56 L <sub>BP</sub> )	8.17 (2.67 L <sub>BP</sub> )	8.29 (2.68 L <sub>BP</sub> )	8.86 (2.90 L <sub>BP</sub> )
Time for yaw 180° (s)	24.20	23.74	24.38	23.15	22.79	23.43
<b>Rudder loads</b>						
-Peak Y force (N)	-4.38	-5.35	-6.48	-5.61	-6.11	-5.76
-Mean Y force (N)	-2.37	-2.86	-2.85	-2.90	-2.80	-3.09
-Peak Z moment (Nm)	6.51	6.44	7.75	6.20	7.66	6.99
-Mean Z moment (Nm)	3.5	3.33	3.29	3.37	3.25	3.65
<b>Hull loads</b>						
-Mean Y force (N)	7.45	7.36	7.63	5.43	6.61	7.32
-Mean Z moment (Nm)	0.01	-0.54	0.49	0.47	0.5	-0.08
<b>Propulsion failure conditions</b>						
Advance (m)	11.87 (3.88 L <sub>BP</sub> )	9.94 (3.25 L <sub>BP</sub> )	10.50 (3.43 L <sub>BP</sub> )	9.78 (3.20 L <sub>BP</sub> )	10.07 (3.29 L <sub>BP</sub> )	11.38 (3.72 L <sub>BP</sub> )
Transfer (m)	4.82 (1.58 L <sub>BP</sub> )	3.51 (1.15 L <sub>BP</sub> )	3.21 (1.05 L <sub>BP</sub> )	3.96 (1.29 L <sub>BP</sub> )	3.83 (1.25 L <sub>BP</sub> )	4.22 (1.38 L <sub>BP</sub> )
Time for yaw 90° (s)	19.64	24.03	22.47	17.55	17.01	18.95
Tactical diameter (m)	-	-	-	-	-	-
Time for yaw 180° (s)	-	-	-	-	-	-
<b>Rudder loads</b>						
-Peak Y force (N)	-1.60	-1.84	-2.57	-1.77	-2.29	-2.37
-Mean Y force (N)	-0.04	-0.09	-0.02	-0.03	-0.05	-0.09
-Peak Z moment (Nm)	2.34	2.15	3.11	2.28	2.92	2.94
-Mean Z moment (Nm)	0.06	0.14	0.02	0.04	0.06	0.13
<b>Hull loads</b>						
-Mean Y force (N)	0.40	0.48	-1.07	0.84	0.48	0.15
-Mean Z moment (Nm)	-0.06	-0.20	-0.22	-0.29	-0.12	-0.26

the normal and propulsion loss conditions can be found in Fig. 12.

The predicted time histories of the ship velocities, motions, forces, and moments during the ship's turning manoeuvre are presented in Fig. 13, in which dotted lines indicate the normal condition and solid lines represent the propulsion failure condition. From Fig. 13, it was observed that the ship in the normal condition experienced the involuntary surge speed loss after the rudder

deflection towards 35° starboard. The speed loss between the initial surge speed and the steady mean value was predicted to range from 48% to 56%, which was due to an increase in ship resistance caused by a large drift angle. The ship in the propulsion loss condition, on the other hand, experienced gradual decreases in the surge velocity after the ship lost its propulsion power and the rudder deflected towards starboard 35°. The propulsion loss was

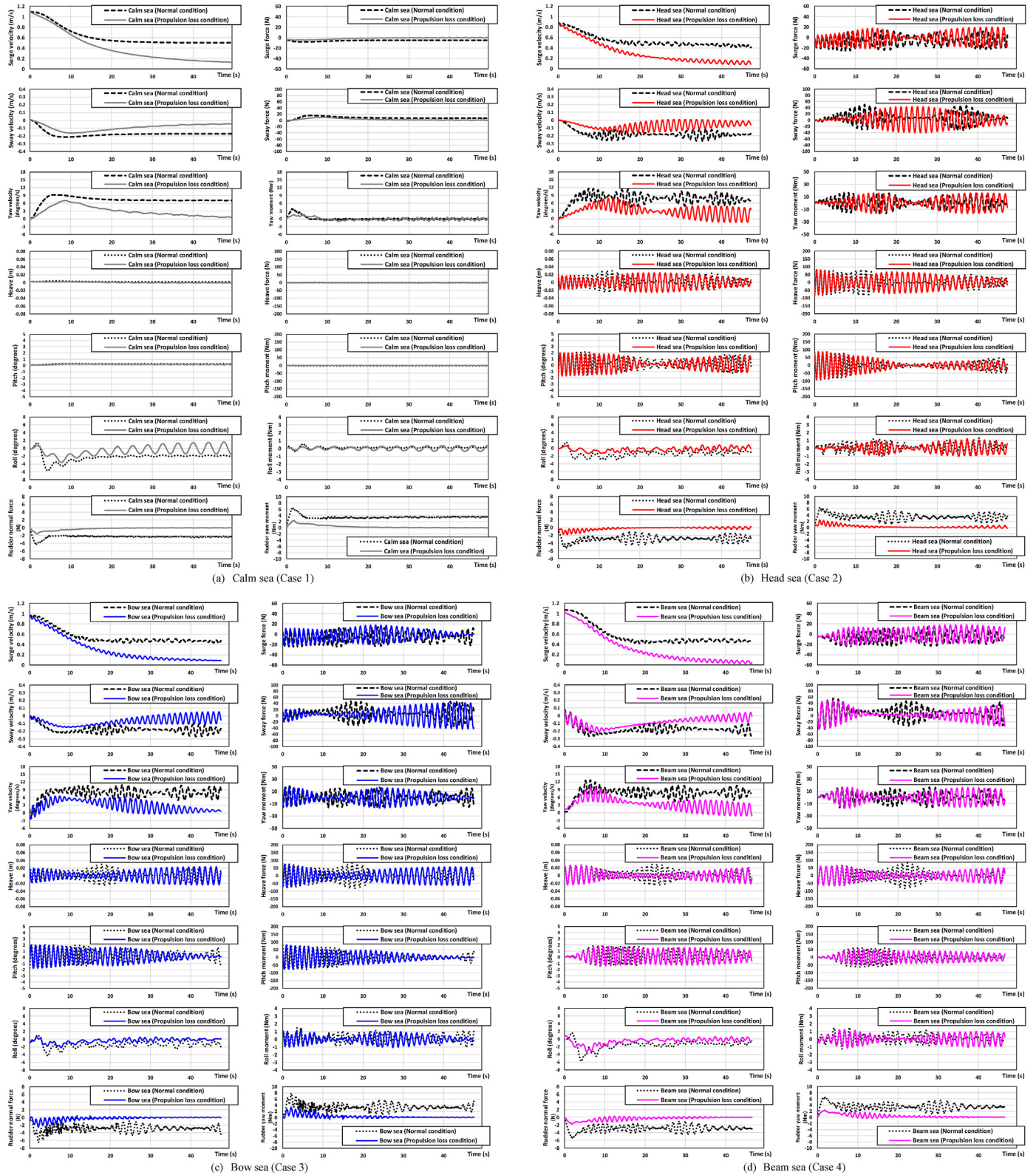


Fig. 13. The time histories of the ship velocities, motions, forces, and moments during the ship's turning manoeuvre.

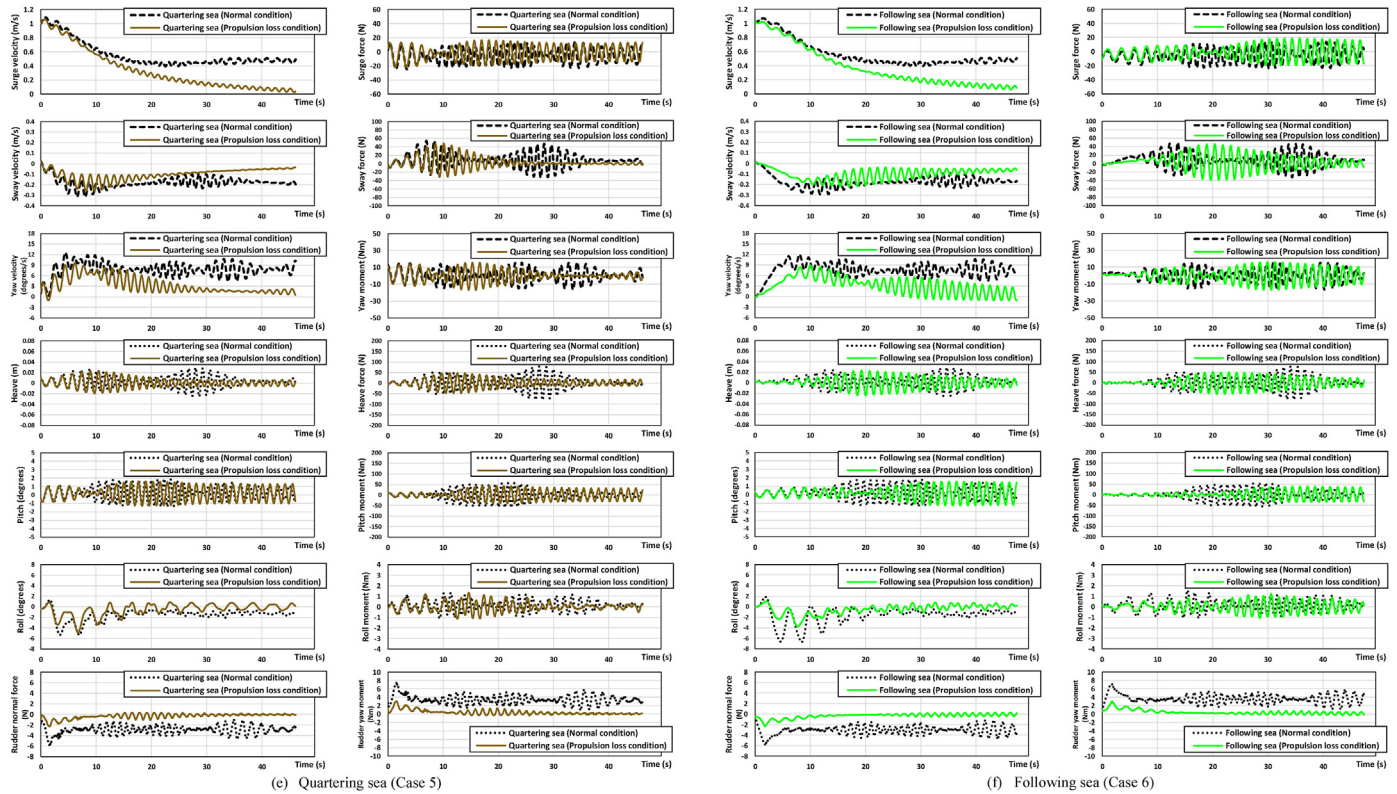


Fig. 13. (continued).

greatly contributed to the speed loss, while increased resistance due to the drift angle accelerated the decrease in the speed. For the sway and yaw velocities, it revealed that they showed a tendency to increase rapidly until a specific time after the rudder deflection and then gradually converged to a certain value in both the normal and propulsion loss conditions. However, such velocities in the propulsion loss condition were found to be noticeably smaller than those in the normal condition. This shows that the greater rudder inflow velocity may lead to the greater rudder normal force, thus causing the relatively large sway and yaw velocities at the beginning of the turning manoeuvre. As for the propulsion failure conditions, it was noted that the ship sailing in the beam, quartering, and following waves achieved the shorter time to turn 90° than the other cases, showing relatively greater yaw rates during the initial transient phase. Such turning behaviour may result from the complicated interaction between the hull, the rudder, and the incident wave after the ship started turning. It has to be stressed that in all propulsion loss cases a 180° turn could not even be achieved during the turning manoeuvre despite the maximum rudder deflection (35°), such that the differences in the ship trajectory between the normal and propulsion loss conditions were remarkable. It was also identified that the ship trajectories were significantly drifted at the end of the turning manoeuvre due to the large speed loss resulted from the propulsion failure. This implies that the ship with the propulsion failure is incapable of executing a large alteration of course to avoid a close-quarter situation within an appropriate time, which may pose a significant threat to navigational safety.

As Table 4 and Fig. 13 jointly show, the differences in the rudder loads are remarkable between the normal and propulsion loss

conditions. During the initial phase of the turn, the maximum of the rudder normal force experienced by the ship in the normal condition was much greater than that in the propulsion loss condition, generating the larger rudder yaw moment. Due to the presence of the surge speed, the ship could generate the rudder normal force and yaw moment to some extent after the propulsion failure. Then, it was found that the ship manoeuvring in the normal condition also exhibited greater average rudder loads when compared with the propulsion loss condition in terms of rudder normal forces and yaw moments during the steady phase of the turn. It has to be pointed out that the rudder normal force and yaw moment experienced by the ship with the propulsion failure was predicted at almost zero during the steady phase, implying that the ship was incapable of performing the turning manoeuvre. The different turning capabilities being ascribed to such differences in the rudder loads affected the hull forces and moments during the turning manoeuvre.

When it comes to seakeeping performance during the turning manoeuvre, except for the calm water case, high-frequency fluctuations in such values occurred in both normal and propulsion loss conditions, which correlated strongly with the wave-induced motions. Such high-frequency wave-induced motions were found to experience continual changes in the frequency of the ship motions, which was attributed to instantaneous variations in the ship surge speed and wave-encounter direction. For example, the ship turning in the quartering waves (case 5) encountered the starboard quartering wave (0° turn), starboard bow wave (90° turn), port bow wave (180° turn), port quartering wave (270° turn), and starboard quartering wave (360° turn) in series after starting the starboard turning manoeuvre. The time histories of the encounter

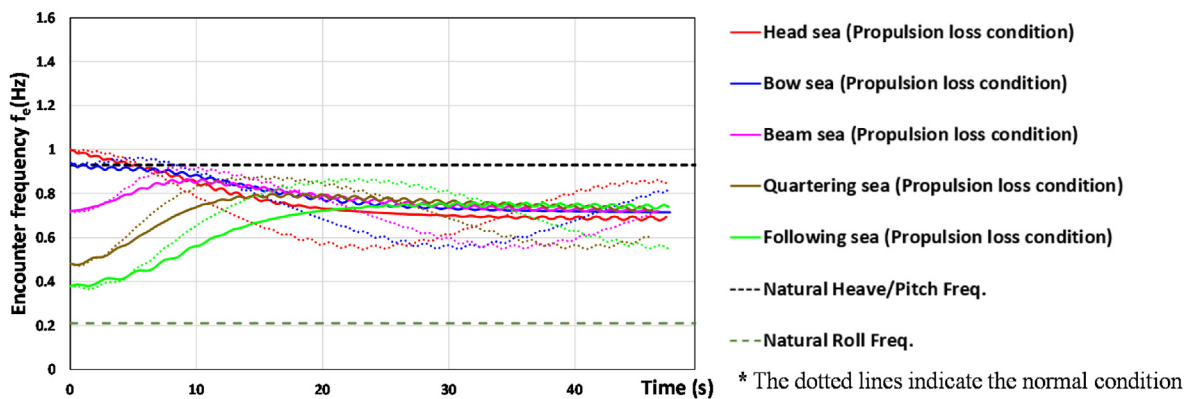


Fig. 14. The time histories of the encounter frequencies during the turning circle manoeuvre in waves.

frequencies during the turning circle manoeuvres in waves are shown in Fig. 14, in which the heave, pitch and roll natural frequencies are also shown. It can be seen that the ship performing a given manoeuvre experienced significant differences in the encounter frequency between the normal condition and the propulsion failure condition. Accordingly, it is expected that the differences in the encounter frequency may lead to differences in seakeeping performance in waves between the normal and propulsion loss conditions.

For the heave motion and force in calm water, there were no recognizable differences between the normal and propulsion loss conditions, as seen in Fig. 13(a). The vertical motion and force were maintained to be almost zero value without any fluctuations while the ship was turning, due to the absence of external disturbances. A similar trend was recognised with respect to the pitch motion and moment for the calm water case. On the other hand, the ship manoeuvring in waves showed identifiable differences in such motions, forces, and moments depending on whether or not the propulsion failure condition was applied. This resulted from a significant difference in the extent of change in the yaw angle and surge speed during the manoeuvre, which affected the change in the encounter frequency and thus the ship motions. The ship under the normal condition experienced the waves coming from all directions during the turning manoeuvre since the 360° turn was achieved within a given period. Because of this, the normal condition showed remarkably continual changes in the encounter frequency (the repetitive increase and decrease in the frequency during the manoeuvre). Contrarily, the propulsion failure condition showed the heading angle variation ranging only from 134° to 159° and relatively small changes in the yaw angle during the turning manoeuvre caused the ship to experience certain wave-encounter directions during the turning, consequently leading to small changes in the encounter frequency (Fig. 14). As for the heave motion, Kim et al. (2021b) state that incident beam waves lead to the maximum heave motion and force, which is closely correlated to the ratio of wavelength to ship length. When the ship experiences the beam waves, the breadth of the ship can be considered as the relevant length that is relatively smaller than the wavelength. Such a small relevant length may cause the maximum vertical motion whose amplitude was almost equal to the incident wave height. Concerning the propulsion loss condition, Case 4 (the beam wave) and 5 (the quartering wave) displayed the maximum vertical motion at the early stage of the turning manoeuvre in which the

ship experienced the starboard beam sea (Fig. 13(d) and (e)). Case 2 (the head wave) and 6 (the following wave) also showed the maximum amplitude of the heave motion at the middle stage of the manoeuvre, in which the ship encountered the beam waves (Fig. 13(b) and (f)). Case 3 (the bow wave) presented the maximum motion at the last stage of the manoeuvre (Fig. 13(c)). Contrary to the vertical motion, it was revealed that the incident beam waves caused the minimum pitch motion during the turning manoeuvre. This may be because the beam waves did not generate considerable differences in pressure between the ship's bow and stern, not causing the pitch moment. The pitch motion at the end of the turning manoeuvre for Case 3 (the propulsion loss condition) can be given as a good example (Fig. 13(c)) in which the pitch amplitude gradually decreased as the wave-encounter angle ( $\mu$ ) became 090° (port beam sea). In addition to this, it was observed that the smaller difference between the encounter frequency ( $f_e$ ) and the natural frequency ( $f_n$ ) led to the increase in the amplitude of the pitch motion, as discussed in the previous sub-section. When it comes to the roll motion, the rudder normal force played an important role in determining the roll motion while the ship was turning. As the rudder was deflected towards the starboard, the ship was first heeled to the starboard (to the centre of the turning circle) due to the generated rudder lift force. Then, the hydrodynamic forces and the centrifugal force acting on the hull caused the ship to heel to the port side (to the outside). From Fig. 13(a)–(f), the ship sailing in the propulsion loss condition showed smaller amplitudes of the roll motion than the normal operating conditions during the manoeuvre for all cases due to the small rudder lift.

Figs. 15 and 16 display the instantaneous free surface elevation around the ship during the turning circle manoeuvre under the normal and propulsion loss conditions, respectively. The free surface elevations around the ship are affected by the interaction of several components including undisturbed incident waves (free waves without consideration of the presence of the ship), diffraction waves (the unsteady perturbation response of the free surface to the presence of the ship), radiation waves (representing the waves generated by the moving ship), Kelvin waves (the wave pattern generated by the advancing ship at non zero forward speed in calm water), and the wake generated by the propeller. It is seen from the figures that the diffraction and radiation waves around the manoeuvring ship are almost invisible due to the coexistence of other effects such as the incident waves and Kelvin waves, as reported in Ohkusu and Wen (1998). Analysis of the radiation and

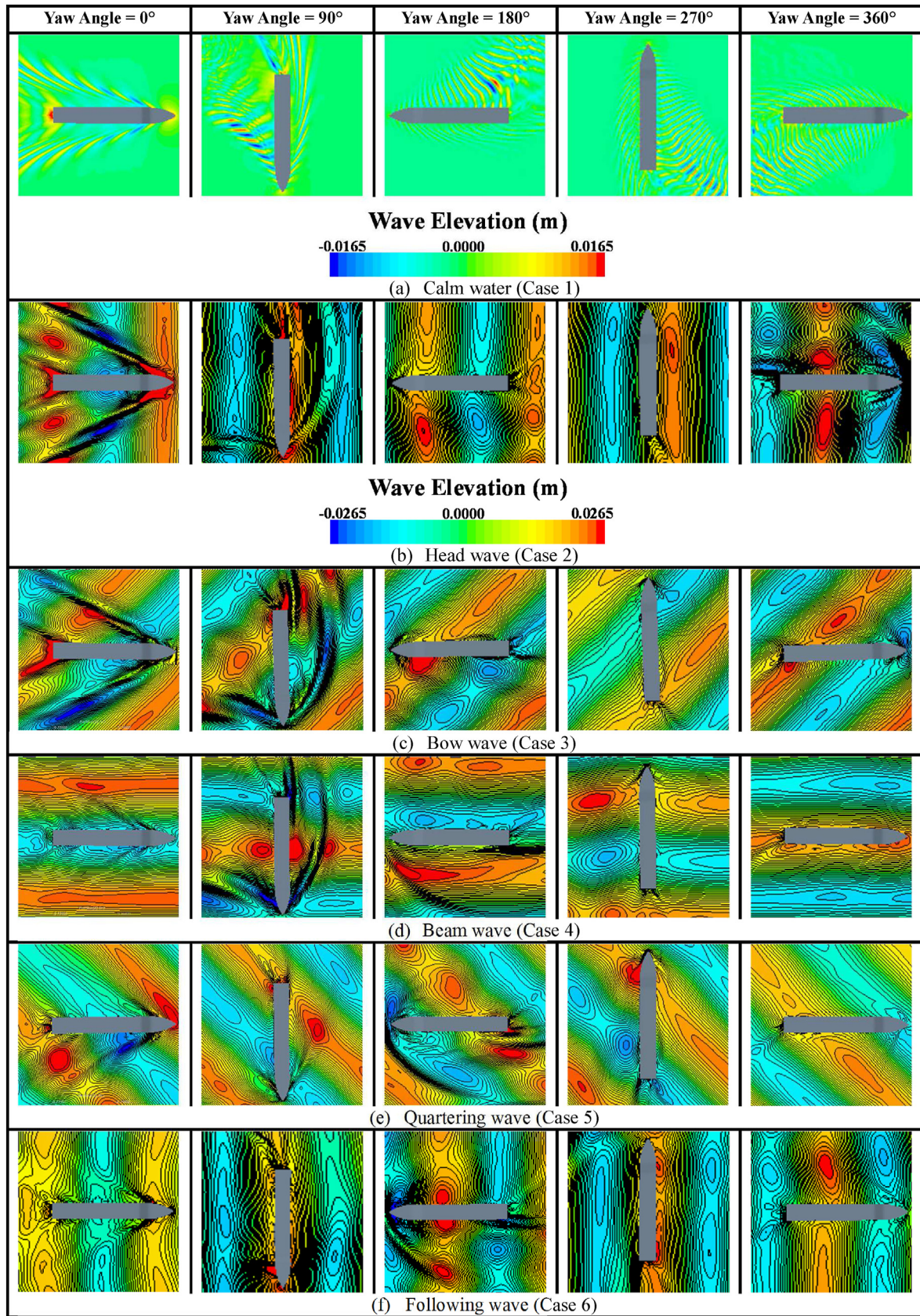


Fig. 15. The free surface elevation during the turning manoeuvre in the normal operating condition.

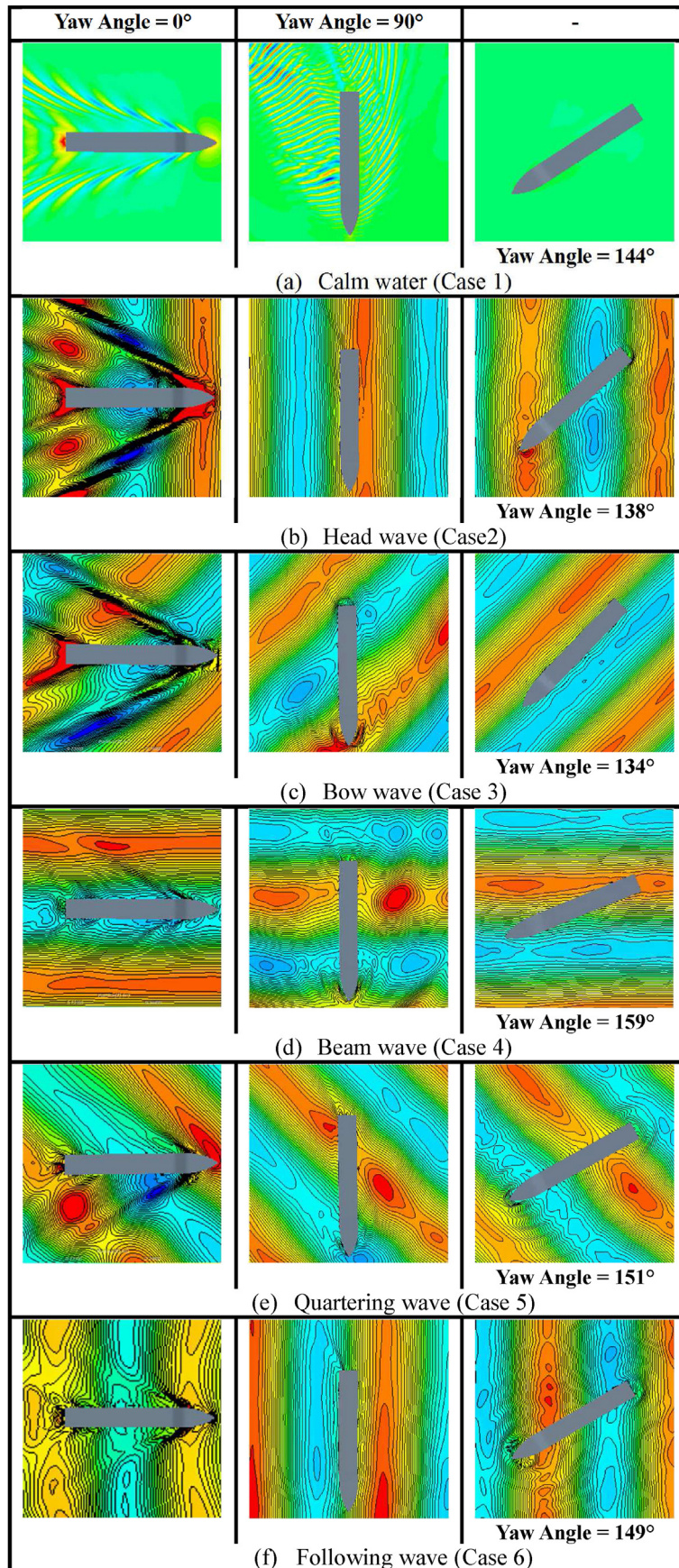


Fig. 16. The free surface elevation during the turning manoeuvre in the propulsion failure condition.

diffraction wave fields generated by the ship was not a focus of this study, so only the instantaneous free surface elevation around the ship was studied. The Kelvin wave generated by the manoeuvring ship was found to have a strong correlation with the surge speed and wave-encounter direction during the turning. The greater the surge speed, the more visible the Kelvin wave generated by the ship becomes. Besides, the generated Kelvin wave seemed quite clear when the ship experienced the waves from the bow during the turning manoeuvre. For the propulsion failure condition, it is observed from the figures that the generated Kelvin wave almost disappeared after the ship lost its propulsion power due to the much smaller surge speed, compared to the normal condition.

#### 4. Conclusions and discussion

This paper has shown the effect of propulsion failure on the course keeping and turning circle manoeuvres under both the normal and propulsion loss conditions. The methodology presented in this study has been applied to the free-running simulations for the KRISO container ship. In examining the ship performances for the normal and propulsion loss conditions, the research findings have demonstrated that the propulsion failure has a significant influence on the course keeping capability, sea-keeping performance, and ship manoeuvrability in a real seaway. The key findings of this research can be summarised as follows:

- 1) The loss of propulsion power strongly affected the heave and pitch responses of the vessel during the course-keeping. This was due to continual changes in the encounter frequency of the wave during the manoeuvre, which resulted from the decreasing surge speed caused by the propulsion loss. It was also found that the yaw angle control based on the PID controller was more challenging in the propulsion failure condition than in the normal condition, such that the rudder deflection became significantly larger after the ship lost its propulsion power. This was associated with the insufficient rudder normal force due to the reduced inflow velocity to the rudder after the propulsion loss. As a result of this, the predicted ship trajectories under the propulsion failure conditions deviated from the planned route much more than that under the normal conditions.
- 2) The turning behaviour of the ship considerably differed according to the presence or absence of the propulsion power, which caused substantial changes in not only the turning trajectories but also the critical manoeuvring indices. It was revealed that the loss of propulsion power led to noticeable increases in the advance, the transfer, and the time to turn by 90° due to the insufficient rudder lift. It is interesting to note that a 180° turn could not even be achieved under the propulsion loss condition, which implies the poor turning ability of the ship. For the seakeeping behaviour during the ship's turning, the ship under the propulsion loss condition presented notable differences in the ship motions, compared to the normal operating condition. This was also attributed to the insufficient rudder normal force, leading to small changes in the ship's heading angle and consequently causing the ship to encounter certain wave-encounter directions during the turning.

COLREGs (International Regulations for Preventing Collisions at Sea, IMO (2001)) state that "the term 'vessel not under command' means a vessel which through some exceptional circumstance is unable to manoeuvre as required by these Rules and is, therefore, unable to keep out of the way of another vessel" in rule 3(f). For this reason, ships suffering from the propulsion failure could be regarded as a vessel not under command as they have poor ship

manoeuvrability. In general, a vessel in the normal operating conditions should, if the circumstances of the case admit, avoid impeding the safe passage of a vessel not under command to prevent collision, due to the better controllability. Nevertheless, navigators, in charge of handling a vessel suffering from propulsion loss, should fully understand the ship's manoeuvrability to determine proper decision-making for ship-handling actions. For example, an emergency anchor operation can be carried out in areas of narrow waterways or shallow water, taking into consideration the poor ship manoeuvrability. In this regard, the manoeuvring results obtained from this study would be helpful for navigators to have a practical insight into the ship manoeuvrability concerning the propulsion failure condition.

This work has furnished a very useful starting point for analyses of ship performances under the propulsion failure condition, especially course keeping and turning manoeuvres in regular waves. In addition to this, this study could further add values by investigating the impacts of adverse sea state conditions on the manoeuvring performance under the normal and propulsion loss conditions as a next step.

#### Declaration of competing interest

The authors declare that they have no known competing financial interests or personal relationships that could have appeared to influence the work reported in this paper.

#### Acknowledgements

Results were obtained using the ARCHIE-WeSt High-Performance Computer ([www.archie-west.ac.uk](http://www.archie-west.ac.uk)) based at the University of Strathclyde. The authors gratefully acknowledge that the research presented in this paper was carried out as part of the EU funded H2020 project, VENTuRE (grant no. 856887).

#### References

- Abkowitz, M.A., 1964. Lectures on Ship Hydrodynamics—Steering and Manoeuvrability.
- Brogli, R., Dubbioso, G., Durante, D., Di Mascio, A., 2015. Turning ability analysis of a fully appended twin screw vessel by CFD. Part I: single rudder configuration. *Ocean Eng.* 105, 275–286.
- Elshiekh, H.A., 2014. Maneuvering Characteristics in Calm Water and Regular Waves for ONR Tumblehome. The University of Iowa.
- EMSA, 2020. Annual Overview of Marine Casualties and Incidents 2020.
- Fenton, J.D., 1985. A fifth-order Stokes theory for steady waves. *J. Waterw. Port, Coast. Ocean Eng.* 111 (2), 216–234.
- Hajivand, A., Mousavizadegan, S.H., 2015. Virtual simulation of maneuvering captive tests for a surface vessel. *Int. J. Naval Architect.* Ocean Eng. 7 (5), 848–872.
- Hasnan, M., Yasukawa, H., Hirata, N., Terada, D., Matsuda, A., 2019. Study of ship turning in irregular waves. *J. Mar. Sci. Technol.* 1–20.
- He, S., Kellett, P., Yuan, Z., Incecik, A., Turan, O., Boulougouris, E., 2016. Manoeuvring prediction based on CFD generated derivatives. *J. Hydrodyn.* 28 (2), 284–292.
- Hirt, C.W., Nichols, B.D., 1981. Volume of fluid (VOF) method for the dynamics of free boundaries. *J. Comput. Phys.* 39 (1), 201–225.
- IMO, 2001. International Regulations for Preventing Collisions at Sea (COLREGs) 1972.
- IMO, 2014. 2013 Interim Guidelines for Determining Minimum Propulsion Power to Maintain the Manoeuvrability of Ships in Adverse Conditions.
- IMO, 2020. PROCEDURES FOR PORT STATE CONTROL, 2019.
- Inoue, S., Hirano, M., Kijima, K., Takashina, J., 1981. A practical calculation method of ship maneuvering motion. *Int. Shipbuild. Prog.* 28 (325), 207–222.
- ITTC, 2011. ITTC - Recommended Procedures and Guidelines : Practical Guidelines for Ship CFD Applications.
- ITTC, 2017. Tasks and Structure of 29th ITTC Technical Committees and Groups, version 4.
- ITTC, 2021. ITTC - Recommended Procedures and Guidelines: Full Scale Manoeuvring Trials.
- Kim, D., Song, S., Jeong, B., Tezdogan, T., 2021a. Numerical evaluation of a ship's manoeuvrability and course keeping control under various wave conditions using CFD. *Ocean Eng.* 237, 109615.
- Kim, D., Song, S., Jeong, B., Tezdogan, T., Incecik, A., 2021b. Unsteady RANS CFD simulations of ship manoeuvrability and course keeping control under various

- wave height conditions. *Appl. Ocean Res.* 117 (2021), 102940.
- Kim, D., Song, S., Tezdogan, T., 2021c. Free running CFD simulations to investigate ship manoeuvrability in waves. *Ocean Eng.* 236, 109567.
- Kim, D.J., Yun, K., Park, J.-Y., Yeo, D.J., Kim, Y.G., 2019. Experimental investigation on turning characteristics of KVLCC2 tanker in regular waves. *Ocean Eng.* 175, 197–206.
- Liu, C., Wang, J., Wan, D., 2020. CFD simulations of self-propulsion and turning circle maneuver up to 90° of ship in waves. *J. Ship Res.* 1–14.
- Liu, Y., Zou, L., Zou, Z., Guo, H., 2018. Predictions of ship maneuverability based on virtual captive model tests. *Eng. Appl. Comput. Fluid Mech.* 12 (1), 334–353.
- Menter, F.R., 1994. Two-equation eddy-viscosity turbulence models for engineering applications. *AIAA J.* 32 (8), 1598–1605.
- Mofidi, A., Carrica, P.M., 2014. Simulations of zigzag maneuvers for a container ship with direct moving rudder and propeller. *Comput. Fluids* 96, 191–203.
- Ohkusu, M., Wen, G., 1998. Radiation and diffraction waves of a ship at forward speed. In: *Proc. Of 21st Symposium on Naval Hydrodynamics*, pp. 29–44.
- Otzen, J., Simonsen, C., 2014. Manoeuvring predictions for the kcs container ship based on experimental and numerical pmm tests. In: *Proceedings of Workshop on Verification and Validation of Ship Manoeuvring Simulation Methods*.
- Paroka, D., Muhammad, A.H., Asri, S., 2017. Prediction of ship turning maneuvers in constant wind and regular waves. *Int. J. Technol.* 8 (3), 387–397.
- Perić, R., Abdel-Maksoud, M., 2018. Analytical prediction of reflection coefficients for wave absorbing layers in flow simulations of regular free-surface waves. *Ocean Eng.* 147, 132–147.
- Romanowski, A., Tezdogan, T., Turan, O., 2019. Development of a CFD methodology for the numerical simulation of irregular sea-states. *Ocean Eng.* 192, 106530.
- Sanada, Y., Elshiekh, H., Toda, Y., Stern, F., 2019. ONR Tumblehome course keeping and maneuvering in calm water and waves. *J. Mar. Sci. Technol.* 24 (3), 948–967.
- Sanada, Y., Tanimoto, K., Takagi, K., Gui, L., Toda, Y., Stern, F., 2013. Trajectories for ONR Tumblehome maneuvering in calm water and waves. *Ocean Eng.* 72, 45–65.
- Seo, M.-G., Kim, Y., 2011. Numerical analysis on ship maneuvering coupled with ship motion in waves. *Ocean Eng.* 38 (17–18), 1934–1945.
- Shen, Z., Wan, D., Carrica, P.M., 2015. Dynamic overset grids in OpenFOAM with application to KCS self-propulsion and maneuvering. *Ocean Eng.* 108, 287–306.
- Shigunov, V., 2019. Assessment of maneuverability in waves. *J. Ship Res.* 63 (2), 78–93.
- Siemens, 2020. *Simcenter STAR-CCM+ Documentation*.
- Simman, 2020. *Workshop on Verification and Validation of Ship Manoeuvring Simulation Methods*.
- Skejic, R., Faltinsen, O.M., 2008. A unified seakeeping and maneuvering analysis of ships in regular waves. *J. Mar. Sci. Technol.* 13 (4), 371–394.
- Subramanian, R., Beck, R.F., 2015. A time-domain strip theory approach to maneuvering in a seaway. *Ocean Eng.* 104, 107–118.
- Tezdogan, T., Demirel, Y.K., Kellett, P., Khorasanchi, M., Incecik, A., Turan, O., 2015. Full-scale unsteady RANS CFD simulations of ship behaviour and performance in head seas due to slow steaming. *Ocean Eng.* 97, 186–206.
- Wang, J., Wan, D., 2018. CFD investigations of ship maneuvering in waves using naoe-FOAM-SJTU Solver. *J. Mar. Sci. Appl.* 17 (3), 443–458.
- Wang, J., Zhao, W., Wan, D., 2016. Self-propulsion Simulation of ONR Tumblehome Using Dynamic Overset Grid Method. Shanghai Jiao Tong Univ. Collaborative Innovation Center for Advanced Ship and Deep-Sea Exploration, USA.
- Wang, J., Zou, L., Wan, D., 2017. CFD simulations of free running ship under course keeping control. *Ocean Eng.* 141, 450–464.
- Wang, J., Zou, L., Wan, D., 2018. Numerical simulations of zigzag maneuver of free running ship in waves by RANS-Overset grid method. *Ocean Eng.* 162, 55–79.
- Yasukawa, H., Hasnan, M., Matsuda, A., 2021. Validation of 6-DOF motion simulations for ship turning in regular waves. *J. Mar. Sci. Technol.* 1–16.
- Yasukawa, H., Yoshimura, Y., 2015. Introduction of MMG standard method for ship maneuvering predictions. *J. Mar. Sci. Technol.* 20 (1), 37–52.
- Zhang, W., Zou, Z.-J., Deng, D.-H., 2017. A study on prediction of ship maneuvering in regular waves. *Ocean Eng.* 137, 367–381.
- Zhang, W., Zou, Z., 2016. Time domain simulations of the wave-induced motions of ships in maneuvering condition. *J. Mar. Sci. Technol.* 21 (1), 154–166.